**RESEARCH ARTICLE**

**Key Points:**
- Enhanced heterogeneous ice nucleation in deep convective clouds with a cold cloud-base temperature may lead to optically thinner anvils
- The impacts of enhanced heterogeneous ice nucleation are especially pronounced when the enhancement occurs at warmer temperatures
- Our findings are likely most applicable to clouds in which warm-rain processes do not contribute much to the total precipitation

**Correspondence to:**
A. Takeishi,
azusa.takeishi@yale.edu

# A Study of Enhanced Heterogeneous Ice Nucleation in Simulated Deep Convective Clouds Observed During DC3

Azusa Takeishi[1] [ID] and Trude Storelvmo[2] [ID]

[1]Department of Geology and Geophysics, Yale University, New Haven, CT, USA, [2]Department of Geosciences, University of Oslo, Oslo, Norway

**Abstract** The impacts of enhanced heterogeneous ice nucleation (HET) on the properties of deep convective clouds (DCCs) have been investigated in cloud-resolving simulations with the WRF-CHEM model. The study focuses on a case observed during the Deep Convective Clouds and Chemistry (DC3) field campaign. For the simulated DCCs, which had cold cloud-base temperatures, an inverse relationship exists between ice crystal mass produced through HET and anvil ice crystal number concentrations. This seems to be due to the indirect competition between HET and subsequent homogeneous freezing (HOM) for liquid droplets. Furthermore, our simulations suggest that HET enhancements at warmer temperatures are more efficient in depleting liquid droplets below and hence have larger impacts on anvil properties than HET enhancements at colder temperatures do. This temperature dependence indicates that similar increases in the number of ice nucleating particles (INPs) may potentially have different impacts on DCCs, depending on the INP type and at which temperatures they can nucleate ice crystals. We also found that the reduced anvil ice number concentrations due to the enhanced HET may lead to optically thinner anvil clouds. The reduction in cloud optical depth comes from a decrease in ice crystal mass concentrations, and in some runs also from an increase in ice crystal sizes. These results suggest potentially large impacts of INPs on the properties of DCCs, especially if precipitation is predominantly produced through ice processes in the DCCs. The results underscore the importance of fully understanding the temperature-dependent ability of aerosol particles to nucleate ice crystals.

## 1. Introduction

The following subsections introduce heterogeneous and homogeneous ice formation mechanisms and their relationships (section 1.1) and present the motivations of this study (section 1.2).

### 1.1. Heterogeneous Ice Nucleation and Homogeneous Freezing

Ice formation in the atmosphere occurs either via heterogeneous nucleation or homogeneous freezing, depending on the ambient temperature and supersaturation; at temperatures above about −38 °C, ice crystals form by heterogeneous nucleation, that is, with the aid of ice nucleating particles (INPs) around which freezing of liquid drops (contact/condensation/immersion freezing) or deposition of water vapor (deposition nucleation) occurs. The heterogeneous ice nucleation (HET) rate is therefore heavily dependent on the existence of INPs, which has a significant temporal and spatial variability. At temperatures below about −38 °C and with sufficient humidity (Kanji et al., 2017), the homogeneous freezing (HOM) process rapidly converts liquid droplets to ice, yielding many relatively small ice crystals. Which of the two mechanisms dominates inside mixed-phase/cold clouds varies from case to case but it is controlled mainly by vertical velocities and INP availability (see Figure 18 in Heymsfield et al., 2005; Figure 4 in Eidhammer et al., 2009; and Figure 1 in Kärcher, 2017): In deep convective clouds (DCCs), higher vertical velocities may lead to higher supersaturation rates that can retain more liquid droplets up to the HOM level (i.e., about −38 °C) and hence make clouds more HOM-dominated. On the other hand, high INP concentrations may enhance HET and make clouds more HET-dominated.

In in situ cirrus clouds, the competition between HOM and HET for moisture is known as the negative Twomey effect (Kärcher & Lohmann, 2003; Kärcher et al., 2006). The transformation of high cirrus clouds into a more
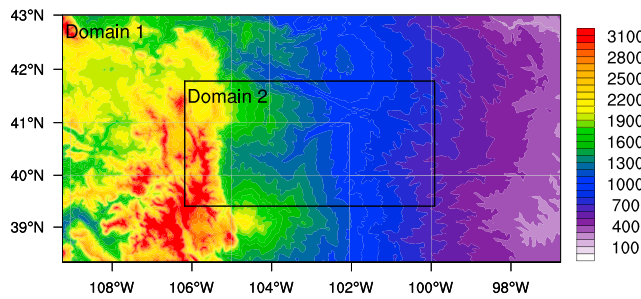
**Figure 1.** Locations of the simulation domains with topography height contours (m) based on MODIS data: Domain 1, outlined by the outer edge of this map, has a 3-km horizontal grid length for the 1,197 km (zonal) × 594 km (meridional) domain and 100 vertical levels. Domain 2, outlined by the black line in the map, has a 1-km horizontal grid length for the 600 km (zonal) × 300 km (meridional) domain and 100 levels.

HET-dominated state with anthropogenic INPs may reduce their warming effect, which has been a topic of intense research among the geoengineering community (e.g., Mitchell & Finnegan, 2009).

In DCCs, however, the relationship between HET and HOM usually cannot be simply explained by the negative Twomey effect: Increases in INPs may occur concurrently with increases in other aerosol particles that can serve as cloud condensation nuclei (CCN). Changes in the abundance of CCN may affect droplet sizes and hence warm-rain processes (e.g., Khain et al., 2008), which in turn influence the availability of liquid droplets for subsequent freezing (either HET or HOM). Also, due to large amounts of condensed liquid, enhanced HET in DCCs may increase latent heat release in the middle/upper troposphere, potentially leading to invigoration of convection. Although it has been proposed to occur due to increased CCN rather than INPs, such invigoration of convection by enhanced freezing has been discussed intensively in recent years (e.g., Altaratz et al., 2014; Fan et al., 2016; Rosenfeld et al., 2008; Tao et al., 2012). This mechanism, however, is still under discussion (e.g., Grabowski & Morrison, 2016; Varble, 2018) and may require further investigations. Furthermore, secondary ice production processes may produce numerous ice crystals in DCCs if temperature, droplet, and ice crystal conditions are favorable (Field et al., 2017), although this remains highly uncertain. Thus, due to warm-rain processes and also secondary ice production processes, HET and HOM may not necessarily *compete* against each other for moisture in DCCs but instead be related in a different way depending on dynamical and microphysical conditions.

Due to high vertical velocities inside DCCs and according to aforementioned studies such as Heymsfield et al. (2005), the dominant ice nucleation mechanism in DCCs is expected to be HOM for the range of typical INP concentrations. Indeed, aircraft measurements by Rosenfeld and Woodley (2000) showed the existence of high concentrations of supercooled liquid droplets near the HOM level inside DCCs. Some modeling studies have found larger impacts of modifying CCN concentrations rather than changing INP abundance on microphysical and dynamical characteristics of DCCs, which indicates the predominant importance of liquid processes and subsequent HOM rather than HET processes. Reisin et al. (1996), for example, presented an idealized modeling study of convective clouds in which various amounts of new droplets or ice crystals, instead of CCN or INPs, were added to the simulated convective cloud at different locations and timings to test how that "seeding" may impact the amount of precipitation. They concluded that additional "INPs" at the right time (i.e., when natural ice formation initiates) may greatly enhance precipitation, though adding "CCN" had overall larger impacts than adding "INPs" did. Similarly, some recent modeling studies have shown a dominant importance of CCN over INPs in determining the microphysical characteristics of DCCs (Carrió et al., 2007; Fan et al., 2010a; Phillips et al., 2007). On the other hand, some modeling studies have shown large impacts of HET on DCC microphysics: A cloud-resolving modeling study by Ekman et al. (2007), for example, found a significant impact of increased INPs on updrafts in a DCC through enhanced freezing and latent heat release. This strengthened updraft in turn increased the areal coverage of the anvil cloud, which is consistent with Fan et al. (2010b), and ultimately increased the total amount of precipitation. Teller and Levin (2006) used 2-D idealized simulations to find a similar expansion of anvil coverage with a tenfold increase in INP concentrations, though they also found that changes in the amount of precipitation depended on the background aerosol concentrations. Hiron and Flossmann (2015) found immersion freezing (one of the HET processes) and HOM to be most important in determining the total number of ice crystals in convective clouds while testing multiple parameterizations in their model. In some of the very few observational case studies on the INP-DCC relationship to date, large impacts of a dust (effective INPs) layer from the Sahara were found based on the data set from the Cirrus Regional Study of Tropical Anvils and Cirrus Layers-Florida Area Cirrus Experiment (CRYSTAL-FACE) (Jensen et al., 2004) in 2002 (Carrió et al., 2007; DeMott et al., 2003; van den Heever et al., 2006); van den Heever et al. (2006), for instance, found that a prescribed increase in the number of INPs at around 3 km in altitude (representing dust plume from the Sahara) in their simulations resulted in increased updrafts during the mature stage and an initial increase in the amount of surface rainfall, due to enhanced glaciation. These studies suggest a potentially very strong influence of INPs on DCCs' microphysical, dynamical, and radiative properties, and thus highlight the potential significance of HET in determining the overall properties of DCCs.

### 1.2. Motivation

Increases in INP abundance may enhance HET in DCCs and eventually modify the anvil properties and surface precipitation. According to a recent review study by Kanji et al. (2017), predominant INP types are biological particles at warmer temperatures ($> -10\,°C$) and dust at colder temperatures ($< -15\,°C$). However, the availability of these INPs is geographically quite heterogeneous and in some regions other aerosol particles, such as biomass burning and marine aerosols, may play a significant role in HET (e.g., DeMott et al., 2016; Kanji et al., 2017; McCluskey et al., 2014).

While it is still debatable, some earlier studies have shown that particles from forest fires may potentially serve as INPs (Hobbs & Locatelli, 1969; Sassen & Khvorostyanov, 2008; Petters et al., 2009; Prenni et al., 2012). Especially a fraction of black carbon (BC), which is also emitted during biomass burning, has been shown in laboratory studies to have a moderate ability to serve as INPs (e.g., DeMott, 1990; DeMott et al., 1999; Diehl & Mitra, 2015). Furthermore, Jolly et al. (2015) found a globally increasing trend in fire season duration in recent decades, and some other observational studies, such as Westerling et al. (2006) and Dennison et al. (2014), found an increasing trend for large fires in the western United States. Using a numerical model, Liu et al. (2013) projected an increase in fire potential and also duration of fires over the United States due to future warming. In addition to aerosols from increasing forest fires including BC, abundant dust particles are also present in the western United States (Achakulwisut et al., 2017; Hallar et al., 2015; Wells et al., 2007). That is, there exist a number of INP sources in the western United States, and therefore, one of our motivations is to investigate how variations in INPs may affect microphysical characteristics of DCCs in this region.

In numerical models, HET is often parameterized by empirically derived equations. These equations, however, vary significantly in terms of their dependence on temperature, humidity, and INP concentrations (e.g., Eidhammer et al., 2009). Here we specifically focus on parameterizations for immersion freezing (IMM), which recent studies have suggested to be the most important HET process in DCCs (e.g., Hiron & Flossmann, 2015; Kanji et al., 2017). Hiron and Flossmann (2015) found changes in the timing and intensity of precipitation from a DCC due to simply switching the IMM parameterization in their simulations. A modeling study by Fan et al. (2010b) compared simulations of DCCs with two INP-independent IMM parameterizations and found that simulations with larger IMM rates produced DCCs with enhanced latent heat release, updraft velocities, and anvil size. Similar results were obtained in a modeling study by Ekman et al. (2007), in which the sensitivity of DCCs to varying INP availability was tested. Thus, even with the identical ambient conditions, simulated HET rates may vary considerably with the choice of parameterization. This potential variation of the results with parameterizations is also investigated in this study.

The present study explores (1) the relative importance of HOM versus HET in the simulated DCCs for a range of different HET/INP profiles and (2) the effects of enhanced HET on the ice-phase microphysics and the optical properties of the DCCs through numerical simulations. Such process studies are indispensable for ultimately disentangling the complex aerosol-DCC interactions with numerical models in the future (see section 5.7 in Rosenfeld et al., 2014). We use different types of HET parameterizations for 3-D cloud-resolving simulations of DCCs observed in Colorado as an example to explore (1) and (2). Besides the aforementioned increasing wildfires, there are multiple reasons to investigate the *simulated* impacts of varying HET rates on DCCs in the western United States, as stated above (e.g., significant variations in HET rates depending on the parameterization). Therefore, rather than modifying INP abundance in the simulations, we directly vary HET rates and intentionally leave the cause of such HET open. They could be attributed to a wide range of reasons (e.g., dust and biological particles). The results of this study may shed light on what changes in microphysical, dynamical, and also radiative characteristics of DCCs might be expected due to modified HET rates for DCCs in the western United States or comparable environments.

The remainder of the paper is structured as follows: Section 2 describes the setup of our numerical simulations (section 2.1), along with the two different types of HET parameterizations applied in the sensitivity tests (section 2.2). The results of the experiments and their analyses are presented in section 3, and the applicability (section 4.1) and implications (section 4.2) of the findings are discussed in section 4. Finally, we summarize the study and draw overall conclusions in section 5.

## 2. Methods

The following subsections describe the setups of the cloud-resolving simulations (section 2.1) and the parameterization of HET for the sensitivity tests (section 2.2).

## 2.1. Cloud-Resolving Simulations by WRF-CHEM

The numerical simulations are carried out by the Weather Research and Forecast (WRF) model (Skamarock et al., 2008) coupled with Chemistry (WRF-CHEM) (Grell et al., 2005) version 3.6.1. We utilize the global anthropogenic emission data set from the REanalysis of the TROpospheric chemical composition over the past 40 years (RETRO) (Schultz et al., 2008) and the Emission Database for Global Atmospheric Research (EDGAR) (http://edgar.jrc.ec.europa.eu) provided by PREP-CHEM-SRC (available at ftp://aftp.fsl.noaa.gov/divisions/taq/global_emissions/) (Freitas et al., 2011), along with the background data produced by the NAL-ROM numerical chemistry model for gases and prescribed initial concentrations for aerosols (see WRF-CHEM user guide for details; http://www2.mmm.ucar.edu/wrf/users/docs/user_guide_V3.6/contents.html). The aerosol scheme for the simulations is the Modal Aerosol Dynamics Model for Europe (MADE) (Ackermann et al., 1998) including the Secondary Organic Aerosol Model (SORGAM) (Schell et al., 2001). The MADE/SORGAM scheme assumes a lognormal size distribution for each of three aerosol modes (Aitken, accumulation, and coarse): The initial geometric mean diameters (GMDs) assumed for background particles are 10 nm (Aitken), 70 nm (accumulation), and 1.0 μm (coarse), whereas the initially assumed *volume* GMD for emitted particles (including fire particles) are 30 nm (Aitken), 300 nm (accumulation), and 6.0 μm (coarse). The volume-weighted bulk hygroscopicity approach is used, which means that particles within the same mode are assumed to be internally mixed and share the same hygroscopicity value, based on the volume ratios of aerosol species. Interaction of aerosols with radiation is turned off for the inner domain in order to isolate microphysical impacts of aerosols. For the calculations of cloud microphysical processes, the Morrison two-moment microphysics scheme (Morrison et al., 2009) is used: HOM occurs instantaneously at $T \leq -40$ °C in the scheme. The parameterizations of HET are explained in detail in the next subsection. Note that the upper limit on the number of ice crystals in the original scheme ($300 \, L^{-1}$) has been eliminated. Also, this scheme uses a saturation adjustment for the calculation of condensed cloud mass, which may potentially be problematic as some studies have shown (e.g., Grabowski & Morrison, 2017). However, assessing this impact is beyond the scope of this study. Other physics and chemistry options chosen for this study are the RRTMG longwave and shortwave radiation schemes (Iacono et al., 2008), the MM5 similarity surface layer scheme (Beljaars, 1995; Dyer & Hicks, 1970; Paulson, 1970; Webb, 1970; Zhang & Anthes, 1982), the unified NOAH land surface model (Tewari et al., 2004), the University of Washington boundary layer scheme (Bretherton & Park, 2009), the RADM2 gas-phase chemical mechanism (Stockwell et al., 1990), and the Guenther scheme for biogenic emissions (Guenther et al., 2006). Photolysis is turned off.

We simulate DCCs observed over northeast Colorado on 22 June 2012 during the Deep Convective Clouds and Chemistry (DC3) field campaign (Barth et al., 2015). The simulation period is 24 hr (from 18 UTC on 21 June to 18 UTC on 22 June) for spin-up and 8 hr (from 18 UTC on 22 June to 02 UTC on 23 June) for analysis. We use adaptive time steps, which start with 18 s (6 s) and may go up to 36 s (12 s) for the outer (inner) domain without any lower limit imposed. The initial and boundary meteorological conditions are provided by the North American Mesoscale Forecast System (NAM) data set with a 12-km horizontal grid length (available at https://www.ncdc.noaa.gov/data-access/model-data/model-datasets/north-american-mesoscale-forecast-system-nam). Figure 1 shows the simulation domains for this study: The outer domain has a 3-km horizontal grid length for the 1,197 km (zonal) × 594 km (meridional) domain, the inner domain has a 1-km grid length for the 600 km × 300 km domain, and the number of vertical levels is 100 for both domains. The analyses presented in this paper focus on the model output from the inner domain, except for the analysis on anvil coverage and cloud albedo. Note that moist air density, instead of dry air density, is used for the conversion of mixing ratios to concentrations in this study, but this is expected to have a minimal influence on the results. Since the area of the simulations (i.e., Figure 1) experienced a number of forest fires during the year of 2012 (e.g., Rippey, 2015), we turn on the forest fire emission input from the Fire Inventory from NCAR (FINN) (Wiedinmyer et al., 2011) data set with a 1-km grid length (turned on after simulation initialization). Fire particles from the FINN are added to the all three modes.

In situ observations of hydrometeors in the size range of 10 to 1,280 μm at a 10-μm resolution by the SPEC Inc. 2D-S (stereo) probe (2DS hereinafter) (Lawson, 2014; Lawson et al., 2006) and also the DC-8 merged data set (Chen et al., 2014) from the DC3 campaign are used as reference data throughout this paper. Also, sounding data from the National Center for Atmospheric Research (NCAR) Mobile Integrated Sounding System (MISS) (UCAR/NCAR [Earth Observing Laboratory], 2013), obtained during the DC3, is used in this paper. These data sets are available on the DC3 website (http://data.eol.ucar.edu/master_list/?project=DC3).

**Table 1**
*Setups of the Simulations Carried Out in This Study*

|    | Name | HET | Description |
|----|------|-----|-------------|
| 1  | HET0[a] | Off | HET rates are set to 0 |
| 2  | B0 |  | Bigg equation $\times$ 0.1 |
| 3  | B1[a] | Based on Bigg (1953) | Bigg equation |
| 4  | B10 | (T < −4°C) | Bigg equation $\times$ 10 |
| 5  | BLO | "BIGG runs" | Bigg equation $\times$ 10 at T $\leq$ −26 °C |
| 6  | BHI |  | Temperature function constant at T > −26 °C |
| 7  | D10_0 |  | D10_1 $\times$ 0.1 |
| 8  | D10_1 | Based on DeMott et al. (2010) | Equation in DeMott et al. (2010) |
| 9  | D10_10 | (−40 °C < T < 0 °C) | D10_1 $\times$ 10 |
| 10 | D10_100 | "D10 runs" | D10_1 $\times$ 100 |
| 11 | D10_1000 |  | D10_1 $\times$ 1000 |
| 12 | D10_10000 |  | D10_1 $\times$ 10000 |
| 13 | D15_0 |  | D15_1 $\times$ 0.1 |
| 14 | D15_1 | Based on DeMott et al. (2015) | Equation in DeMott et al. (2015) |
| 15 | D15_10 | (−40 °C < T < 0 °C) | D15_1 $\times$ 10 |
| 16 | D15_100 | "D15 runs" | D15_1 $\times$ 100 |
| 17 | D15_1000 |  | D15_1 $\times$ 1000 |
| 18 | D15_10000 |  | D15_1 $\times$ 10000 |
| 19 | ALL[a] | Freeze all droplets (T < −4 °C) | Instantly convert all droplets to ice |

[a]An additional simulation has been carried out over a slightly shifted domain (section 2.2).

### 2.2. Parameterization of Heterogeneous Ice Nucleation

As recently reviewed by Kanji et al. (2017), there are mainly two types of parameterizations for HET: time dependent ("stochastic") and time independent ("deterministic"). In this study we test the sensitivity of DCCs to varying HET rates using both types.

The parameterization of IMM by Bigg (1953) is time dependent and used for the first set of the simulations. It is embedded in the original Morrison microphysics scheme (Morrison et al., 2009) that all of the simulations in this study employ. The Bigg parameterization provides IMM *rates* for the temperature range of T < −4 °C that subsequently get multiplied by the lengths of time steps. This parameterization, however, has been shown to produce unrealistically high numbers of ice crystals according to Khain et al. (2000). Nevertheless, it is still frequently used in cloud microphysics schemes. It should also be noted that the Bigg parameterization is INP independent: Its formulation is a function of temperature and liquid droplet mass and number, but not a function of INP concentrations. This is equivalent to assuming perpetual INP supply in the atmosphere, which is unlikely to occur in reality. For the sensitivity tests using this parameterization, the Bigg equations (for both mass and number) are multiplied by 0.1 and 10 (called "B0" and "B10" hereinafter, respectively). These simulations are compared to a baseline simulation without any modification ("B1"). In other runs, HET is enhanced only for a cold ($\leq$ −26 °C, "BLO") or warm (> −26 °C, "BHI") temperature range. These simulations are carried out in order to test the dependence of the impacts of HET enhancement on the temperatures at which HET is enhanced. Table 1 lists the descriptions of the simulations. Even though HET in the runs using the Bigg parameterization (these are called the "BIGG runs" hereinafter) is not based on INP concentrations, these simulations reveal (1) the impacts of varying HET rates especially prominent at cold temperatures due to the strong temperature dependence of the equation and (2) their dependence on altitudes at which HET is most enhanced.

In contrast to the Bigg parameterization, the HET parameterization by DeMott et al. (2010) is time independent and INP dependent. This DeMott parameterization predicts a number concentration (not a *rate*) of INPs based on temperature and the concentration of aerosol particles larger than 0.5 μm. In this study, we use this equation while assuming the following: (1) Newly nucleated ice crystals have a radius of 10 μm, and (2) lognormal size distributions apply not only to interstitial aerosols but also to in-hydrometeor (wet) aerosols.
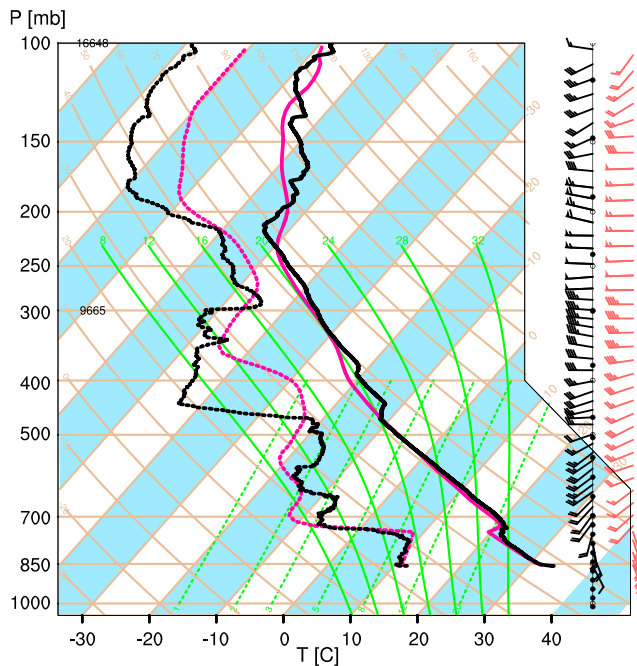
**Figure 2.** Observed (black) and simulated (red) profiles of temperature (solid), due point temperature (dotted), and wind (wind barb) in a skew-T log-P diagram: Observation was made at (lat, lon) = (40.329, −103.806) at 1856 UTC by the NCAR MISS sounding (UCAR/NCAR [Earth Observing Laboratory], 2013) on 22 June 2012 during DC3, whereas the simulation data is from the HET0 run at (lat, lon) = (40.3302, −103.805) at 1900 UTC on 22 June.

The baseline simulation is named D10_1. In additional simulations, HET is forced to be either weakened or enhanced by multiplying the entire equation in DeMott et al. (2010) by 0.1, 10, 100, 1,000, and 10,000 ("D10_01," "D10_10," "D10_100," "D10_1000," and "D10_10000"). Such a variety of enhancements are able to cover a wide range of INP concentrations available in the atmosphere. It is especially relevant here given the finding of McCluskey et al. (2014) that the parameterization by DeMott et al. (2010) underestimated INP concentrations in the presence of wildfires. In the simulations based on the equation by DeMott et al. (2010) (or the "D10 runs"), HET occurs within the temperature range of −40 °C < T < 0 °C. Note that if ice crystals already exist, their number concentrations are subtracted from what is predicted by the equation of DeMott et al. (2010) (or its product with factors above) to obtain the number of newly nucleating ice crystals. Also, the number of newly nucleated ice crystals is constrained not to exceed the number of liquid droplets available to freeze. Since these calculations give number *concentrations*, the HET *rates* are obtained by dividing the number of newly nucleated ice crystals by the length of time steps. The D10 simulations represent a variety of HET rates consistent with the wide range of INP concentrations possible in the atmosphere and reveal their relation to DCC microphysical properties. In order to evaluate the robustness of the results, an identical set of simulations but with the equation of DeMott et al. (2010) replaced by the one in DeMott et al. (2015) have been carried out (the "D15 runs"). The equation in DeMott et al. (2015) parameterizes the dependence of the number of INPs on the abundance of dust particles larger than 0.5 μm. In this study, number concentrations of *all* particles (not only dust) that are ≥ 0.5 μm in the accumulation and coarse modes are used for the calculation. Because the HET parameterization for the D15 runs is quite similar to that for the D10 runs in this case, the D15 simulations are mainly used for checking the robustness of the results in the D10 runs.

In all of the runs, any other primary ice nucleation processes, such as contact freezing and deposition nucleation, are turned off (i.e., their rates are set to 0). This is justified by the findings from Hiron and Flossmann (2015) and also Kanji et al. (2017) that IMM is the dominant ice nucleation process in mixed-phase clouds. We also run two extreme simulations in which any HET processes are set to zero ("HET0") or all droplets instantly turn into ice crystals at T < −4 °C ("ALL"). These simulations represent extremes that are used for assessing the relative importance of HET and HOM in the BIGG runs and the D10/D15 runs. Likely due to the extremely unrealistic assumption, however, the ALL simulation terminated at about 2300 UTC on 22 June due to numerical instability, and hence, the analysis time for the ALL run is shorter than that for the other simulations. To evaluate the robustness of the results, simulations with slightly shifted domains (i.e., moved eastward by 0.01°) have been carried our for HET0, ALL, and B1. The results from these simulations are shown in selected figures. The simulations conducted for this study are listed in Table 1.

## 3. Results

The DCCs of interest developed in a relatively dry environment, as Figure 2 shows. As a result, the cloud-base temperature is close to the 0 °C level and the fully liquid part of the clouds (i.e., T ≥ 0 °C) is therefore expected to be shallow.

Throughout the paper, "convective cores" are defined as grid boxes with vertical velocity $w$ ≥ 1.0 m/s and water content (liquid droplets + ice crystals) ≥ 0.1 g/m³, and "convective anvils" as grid boxes with water content (liquid droplets + ice crystals) ≥ 0.001 g/m³ at T ≤ −40 °C (excluding convective cores), referring to Giangrande et al. (2016) and Table 1 in Hess et al. (1998). Figure 3 shows the cumulative numbers of grid boxes categorized as (a) "convective cores" and (b) "anvils" in the BIGG runs (qualitatively similar results are obtained from the D10 and D15 runs, while not shown here). Except for ALL, the numbers of "convective cores" show their peaks at around 11.5 km, which is the altitude of spreading anvil clouds (Figure 3b). This indicates that some grid boxes that are somewhat away from the center of vigorous convective cores may be categorized
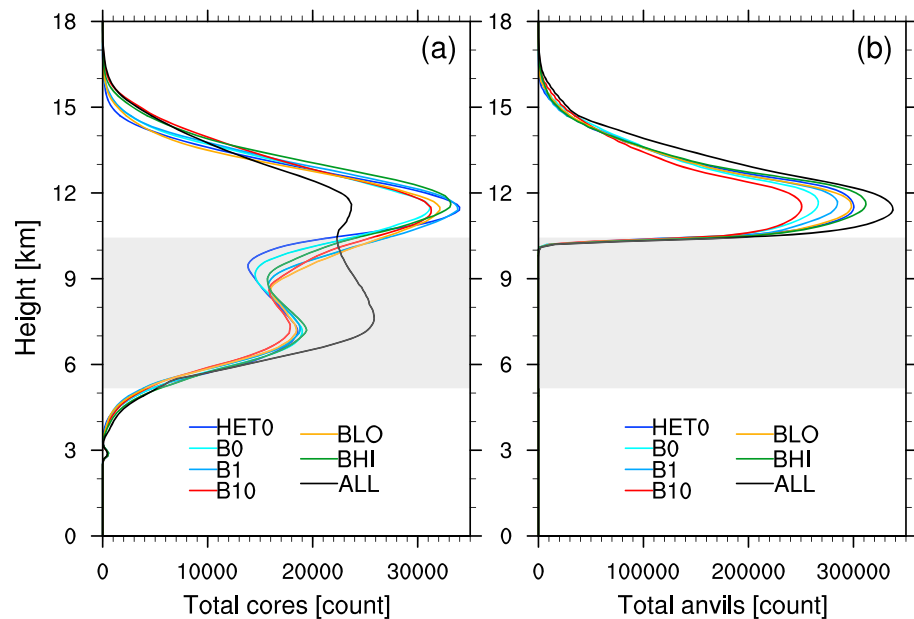
**Figure 3.** Cumulative numbers of grid boxes that are categorized as (a) convective cores and (b) anvils in the BIGG runs between 20 and 23 UTC on 22 June. The average altitudes of mixed-phase temperature range inside convective cores in HET0 are indicated by gray shading. These profiles are vertically interpolated at every 100 m.
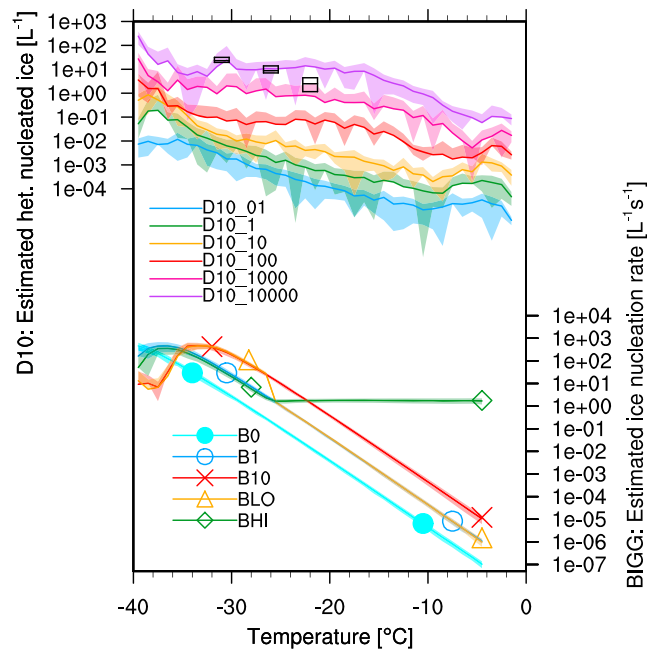


**Figure 4.** Estimated number concentrations of heterogeneously nucleated ice crystals ($L^{-1}$) in the D10 runs (top, left axis) and estimated HET rates ($L^{-1}$/s) in the BIGG runs (bottom, right axis) averaged between 20 UTC on 22 June and 00 UTC on 23 June (10-min interval), along with their ± temporal standard deviation (shading; its lower half is not shown if its lower edge is a non-positive value). These are estimated from the model output, instead of directly output by the simulations, for the grid boxes of "convective cores." As a reference, ground-based observational data of INPs from Table 1 of McCluskey et al. (2014) is shown with boxes (the reported data were for standard temperature and pressure, and hence, an approximate density correction has been performed, using mean temperature and pressure data at about −22.29, −26.04, and −30.67 °C in HET0). This observational data and simulated ice crystal number concentrations are directly comparable if there is no preexisting ice crystals in the simulations, since preexisting ice number concentrations are subtracted from what is predicted by the equation in DeMott et al. (2010) to obtain the number of newly nucleated ice crystals that is shown in this figure. In order to obtain the rates for the BIGG runs, approximate lengths of the simulation time steps were used (e.g., a time step length at 20 UTC is used for estimating the nucleation rates between 20 UTC and 2050 UTC).
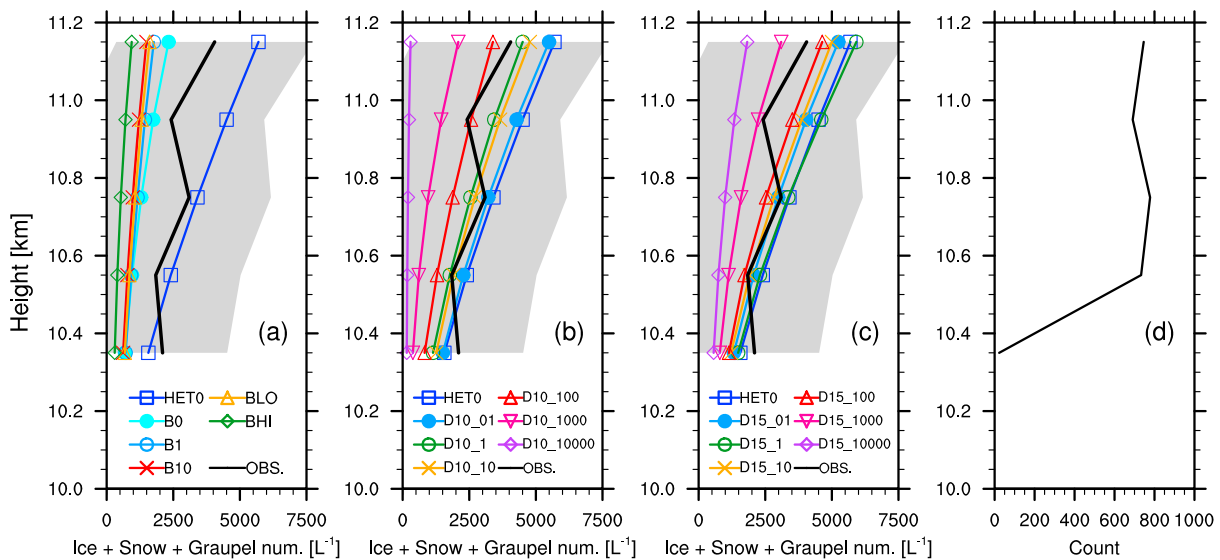
**Figure 5.** Hydrometeor number concentrations (L$^{-1}$) observed by the 2DS (black) during the flight on 22 June, along with their ± standard deviation (shading), and simulated mean frozen hydrometeor (ice + snow + graupel) number concentrations (L$^{-1}$) in the (a) BIGG, (b) D10, and (c) D15 runs. The observed data come from the 2DS measurement on 22 June during the DC3, only at T ≤ −40 °C and ice water content ≥0.001 g/m$^3$ to avoid liquid droplets and cloud-free data, respectively. For the simulated data, the sum of ice, snow, and graupel masses/numbers, horizontally averaged between 20 UTC on 22 June and 02 UTC on 23 June (10-min interval), is used. The ALL run is not included in this figure, due to the lack of data for the last 3 hr. Any simulated data points with T > −40 °C or out of the vertical velocity or altitude range measured on DC-8 are excluded. Furthermore, simulated data points with water content <0.001 g/m$^3$ or above the maximum ice water content observed by the 2DS are also excluded. Since our simulations have approximately 200-m vertical grid interval around this height, the 2DS data are binned into five 200-m bins (10.25–10.45, 10.45–10.65, 10.65–10.85, 10.85–11.05, and 11.05–11.25 km) and averaged within each bin. On the other hand, the simulated data are vertically interpolated at five altitude levels (10.35, 10.55, 10.75, 10.95, and 11.15 km). The total count of valid 2DS data in each of the five bins is shown in (d).

as "convective cores", as long as water content is high enough (e.g., thick anvils) and some updraft exists (e.g., gravity waves, see some wave-like patterns in Figure S1 in the supporting information). The ALL run has fewer "convective cores" around the anvil height due to generally lower ice mass concentrations as shown later in section 3.3. Thus, the potential contribution of thick anvils to "convective cores" must be kept in mind in this study when the data from "convective cores" around 11.5 km is considered. The larger numbers of "convective-core" grid boxes in the ALL run between 6 and 10 km are likely because of extremely efficient ice nucleation followed by the growth of ice, which may increase the number of grid boxes with water content ≥ 0.1 g/m$^3$ (see Figure S2 for generally increased cloud cover between 6 and 10 km in ALL).

The following subsections present the impacts of enhanced HET on the microphysical properties of the DCCs in the BIGG runs (section 3.1) and the D10/D15 runs (section 3.2), and the resultant impacts on the radiative properties of the DCCs (section 3.3).

### 3.1. Microphysical Impacts of Enhanced HET in the BIGG Runs

Figure 4 (bottom, right axis) shows the approximate HET rates in convective cores, estimated from the simulation output of the BIGG runs. Except for temperatures near −40 °C, ice nucleation rates show almost a simple tenfold increase from B0 to B1 and B1 to B10. The comparison of their results, therefore, simply provides the impacts of enhanced HET at all temperatures. On the other hand, the comparison of BLO and B1 (or BHI and B1) shows the impacts of enhancing HET only at cold (or warm) temperatures.

Validation of the simulated results against observations is not trivial for the DCCs of interest, since in situ measurements inside convective cores are not available. Figure 5a shows the observed and simulated hydrometeor number concentrations at T ≤ −40 °C, within the same ranges of ice water content and vertical velocities. All of the profiles in the BIGG runs lie within the ± standard deviation of the 2DS observation. Although this suggests that the simulated cloud properties may be similar to the observation, the spatial and temporal coverage of the observational data is limited (Figure 5d), and therefore we cannot conclude how well our simulations represent the specific DCCs observed on 22 June. For this reason, this study aims to investigate the simulated impacts of enhanced HET on DCCs that develop in a realistic environment over the
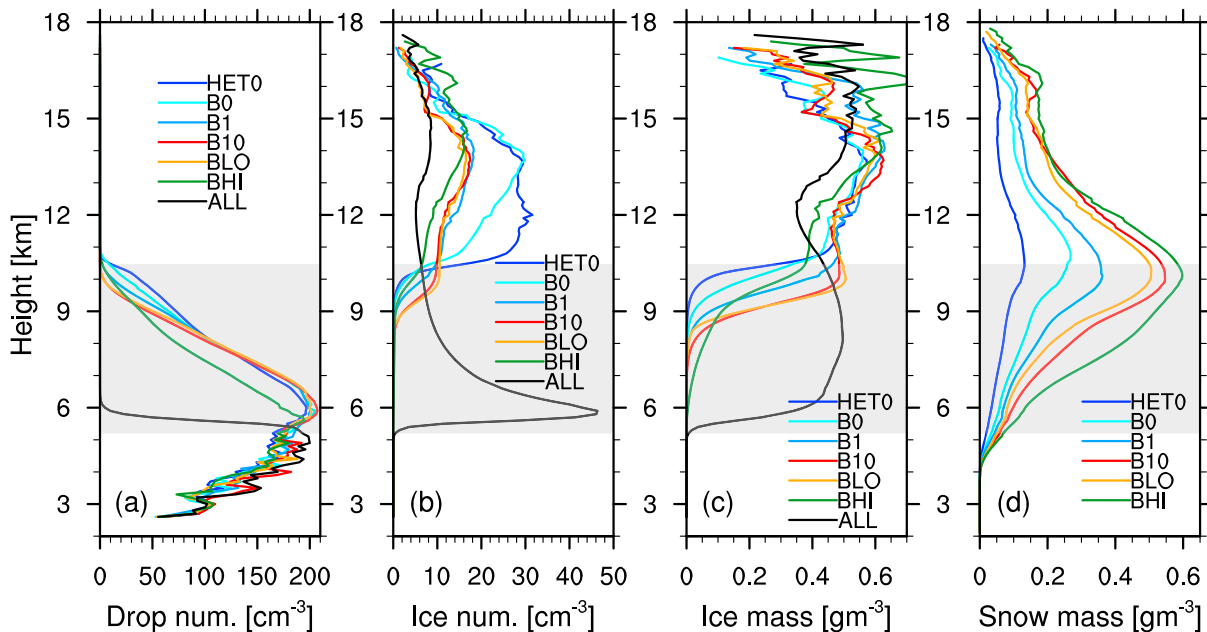
**Figure 6.** Mean vertical profiles of (a) liquid droplet number (cm$^{-3}$), (b) ice number (cm$^{-3}$), (c) ice mass [g/m$^3$], and (d) snow mass (g/m$^3$) concentrations, averaged between 20 UTC and 23 UTC on 22 June (about early development stage) for (a)–(c) and 20 UTC on 22 June and 02 UTC on 23 June (includes later in storm lifetime) for (d). Note that (d) does not have ALL due to the lack of data for the last few hours of the run. These are all averages inside "convective cores" (see text for the definition). The average altitudes of mixed-phase temperature range inside convective cores in HET0 are indicated by gray shading. These profiles are vertically interpolated at every 100 m.

area, but the simulations are not suited to *quantitatively* assess the actual impacts on the specific DCCs on 22 June 2012.

Figure 6 shows mean vertical profiles of key hydrometeor mass/number concentrations inside convective cores averaged from 2000 UTC to 2300 UTC on 22 June (relatively early in the storm development) for droplets and ice and from 2000 UTC on 22 June to 0200 UTC on 23 June (includes later in the storm lifetime) for snow. According to this figure, ALL is clearly an extreme case, whereas HET0 is similar to some of the other simulations, especially in terms of droplet numbers (Figure 6a) and ice mass (Figure 6c). This indicates that ice crystals in the BIGG runs are produced mainly through HOM rather than HET, though this dominance of HOM clearly varies with HET rates below. This is evident from Figure 6b which shows significant increases in ice number concentrations at around 10.5 km near the HOM level and also a large variation aloft. In Figure 6, it is clear that B10 and BLO are quite similar. Because of the strong temperature dependence of the Bigg equation (e.g., Figure 4), most of the enhancement effect in B10 and BLO comes from the enhanced HET at cold temperatures. When the enhancement at warm temperature is strong enough as in BHI, however, significant differences relative to B1 are evident, especially in snow mass (Figure 6d). Snow mass systematically increases as HET is enhanced, and shows an especially large increase when HET is enhanced at warm temperatures as in BHI. This emphasizes the importance of the altitude at which INP enhancement occurs in determining the overall response of the storm.

In order to further reveal the relationship between HET processes and the properties of the convective anvils, we investigate ice crystal number concentrations in the convective anvils in relation to multiple cloud variables inside the convective cores (Figures 6b and 6c show very small ice mass/number below 9 km in HET0, which means that below this height we can expect very small impacts of ice crystals falling from above after HOM). Figure 7a shows the relationship between ice crystal number concentrations below 9 km in convective cores and ice crystal numbers in anvils. Even though it generally shows an inverse relationship between the two variables, it should be noted that HET0 has a nonzero ice number below 9 km, which must be due to falling ice crystals. The inverse relationship becomes even clearer for ice crystal mass below 9 km in Figure 7d. From these figures, it is evident that HOM and HET have an inverse relationship due to their indirect competition for droplets. Indeed, anvil ice number concentrations generally increase as droplet number concentrations in convective cores increase (Figure 8a). Mean snow mass shown in Figure 8d increases as HET is enhanced
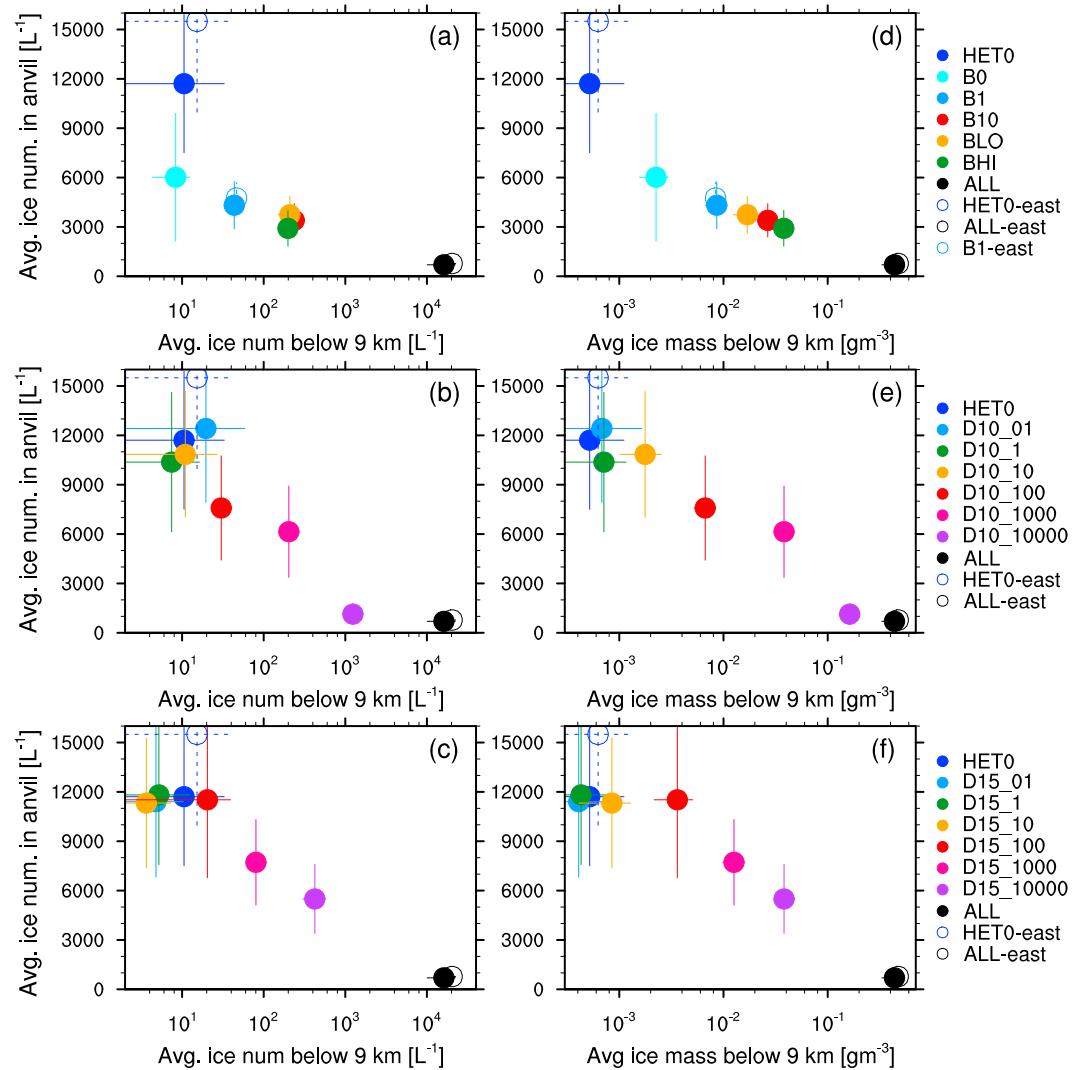
**Figure 7.** Mean ice (a–c) number (L$^{-1}$) and (d–f) mass (g/m$^3$) concentrations inside convective cores below 9 km (*x*-axis), plotted against mean ice number concentrations (L$^{-1}$) in convective anvils (*y*-axis) for the (a and d) BIGG, (b and e) D10, and (c and f) D15 runs. These are averages between 20 UTC and 23 UTC on 22 June (10-min interval), along with their ± temporal standard deviation indicated by lines. The original data are vertically interpolated at every 100 m before the averaging. The results from the simulations with shifted domains (section 2.2) are shown by the hollow circles ("-east").

and anvil ice number concentrations decrease, which is similar to ice mass below 9 km (Figure 7d). Therefore, as HET is enhanced, ice mass at warmer temperatures and overall snow mass increase, which enhances droplet depletion and reduces ice crystal number concentrations in the anvil since HOM is (not completely but) more suppressed. This may be the reason why ice crystal mass (Figure 7d) rather than ice crystal numbers (Figure 7a) shows a clearer inverse relation to anvil ice numbers, as depletion of liquid droplets occurs mainly due to ice crystal (and snow) growth by riming and the Wegener-Bergeron-Findeisen process (represented by ice mass) rather than HET itself (represented by ice numbers). Furthermore, these effects of enhanced HET are more "efficient" if the enhancement takes place at warmer temperatures: Vertically integrated ice nucleation rates are higher in BLO or B10 than those in BHI (Figure 4), and yet the earlier nucleation of ice (i.e., at warmer temperatures) in BHI allows for greater growth of ice and snow at the expense of liquid droplets (Figures 6a and 8a).

Changes in the amounts of precipitation with increasing HET rates are, however, not as systematic as ice and snow (Figure 9d). This is likely because of nonlinear changes of graupel mass with HET rates (Figure 9a), which may result from the combination of multiple variables that change simultaneously with enhanced
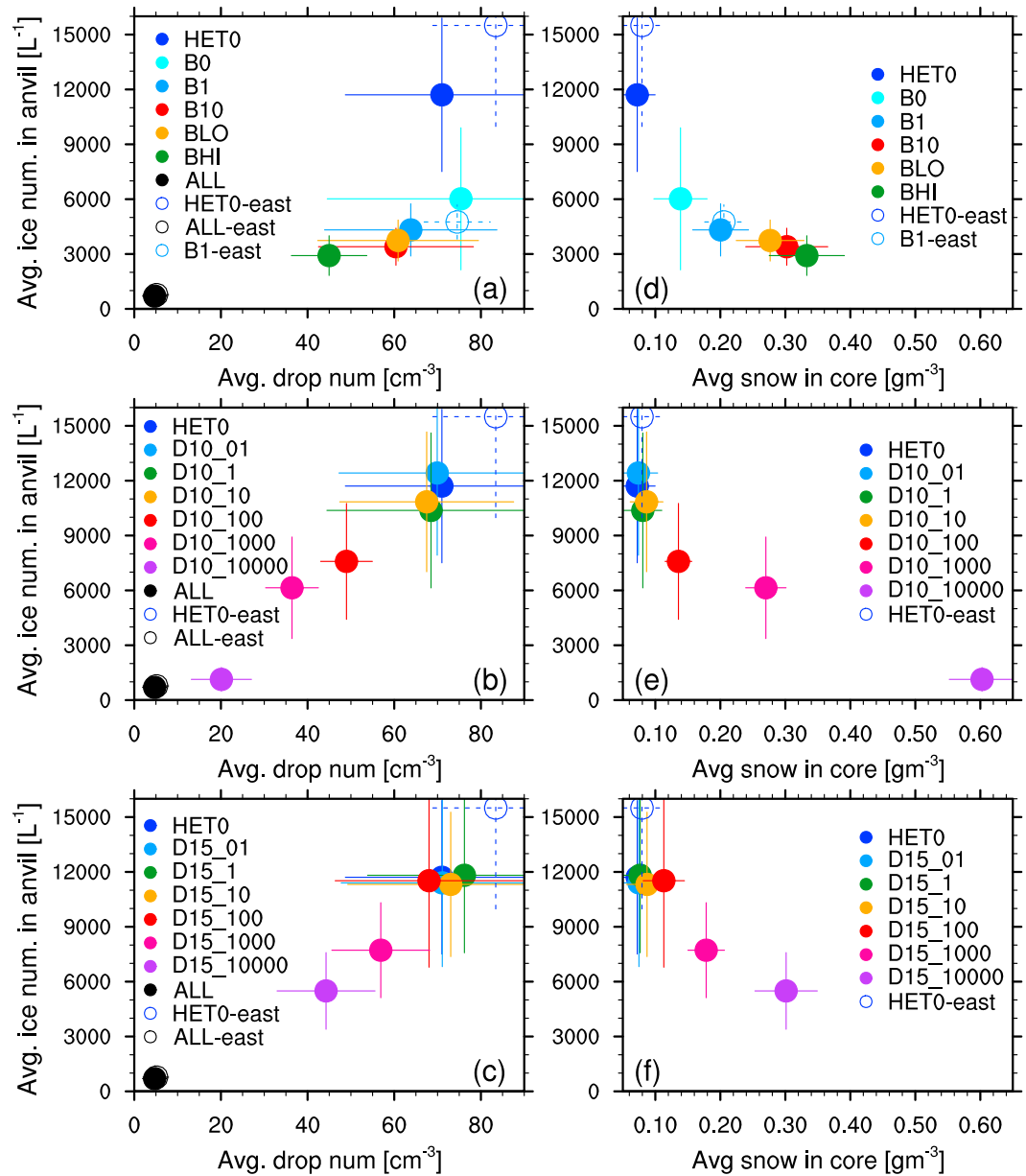
**Figure 8.** Same as Figure 7 but with mean (a–c) droplet number concentrations ($cm^{-3}$) and (d–f) snow mass concentrations ($g/m^3$) both in convective cores on the x-axis. Note that the snow mass concentrations are averaged between 20 UTC on 22 June and 02 UTC on 23 June.

HET and have competing effects on graupel production, such as the abundance of snow and droplets. Note that the anvil ice number concentrations presented in Figures 7–9 are highly correlated with ice number concentrations in convective cores above 11 km (e.g., Figure 6b), as shown in Figure S3. Also, snow mass concentrations inside convective cores represent its domain-mean mass well, and hence, its relation to anvil ice number concentrations still holds even when Figures 8d–8f are plotted against the domain-mean snow mass instead of in-core averages (Figures S4a–S4c). In the same manner, the unsystematic response of in-core graupel mass (Figures 9a–9c) is also seen even if domain-mean graupel mass is plotted instead (Figures S4d–S4f).

The simulations with shifted domains show very similar tendencies in Figures 7–9. Furthermore, very similar results are obtained even when frequency-based averaging (i.e., sum of all data divided by the total number of grid boxes integrated over time), instead of temporal averaging (as in Figures 7 and 8), is done (see
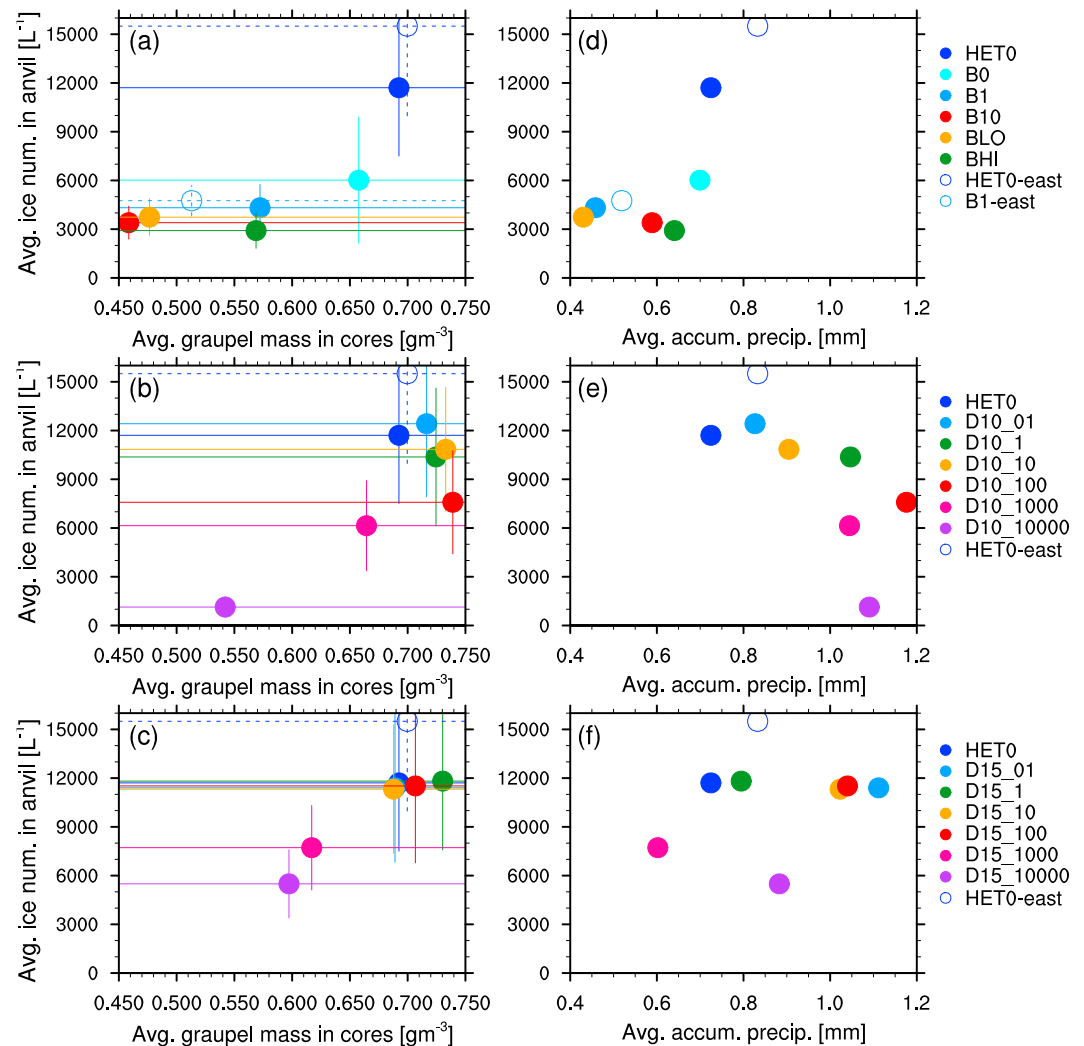
**Figure 9.** Same as Figure 7 but with (a–c) mean graupel mass concentrations (g/m³) in convective cores averaged between 20 UTC on 22 June and 02 UTC on 23 June and (d–f) domain-average accumulated surface precipitation between 18 UTC on 22 June and 02 UTC on 23 June (mm) on *x*-axis.

Figures S5 and S6). In other words, the results are robust both to the choice of averaging methods and to small perturbations of the cloud dynamics.

### 3.2. Microphysical Impacts of Enhanced HET in the D10/D15 Runs

As introduced in section 2.2, heterogeneously nucleated ice crystal number *concentrations*, rather than *rates*, are calculated in the D10 runs according to INP availability. Figure 4 (top, left axis) shows estimated ice crystal number concentrations (in convective cores) produced through HET in the D10 runs: the temperature dependence is much weaker than that in the BIGG runs, and the enhancement of HET is comparable across all temperatures. The ground-based INP observations by McCluskey et al. (2014) lie between D10_1000 and D10_10000 (Figure 4), and hydrometeor concentrations in D10_1 and D10_10 seem to match relatively well with what was measured in situ by the 2DS (Figure 5b). Figure 10 shows vertical profiles of droplet and ice numbers and ice and snow masses for the D10 runs, all inside convective cores. As in the BIGG runs, droplet number concentrations in the convective cores and ice crystal number concentrations above the HOM level decrease as HET is enhanced (Figures 10a and 10b). On the other hand, ice mass below the HOM level and snow mass seem to increase with HET enhancement (Figures 10c and 10d), as expected. These relationships are even clearer in Figures 7b, 7e, 8b, and 8e. That is, enhanced HET increases ice below the HOM level and snow mass, which leads to more depletion of liquid droplets available for subsequent HOM. As a result, ice
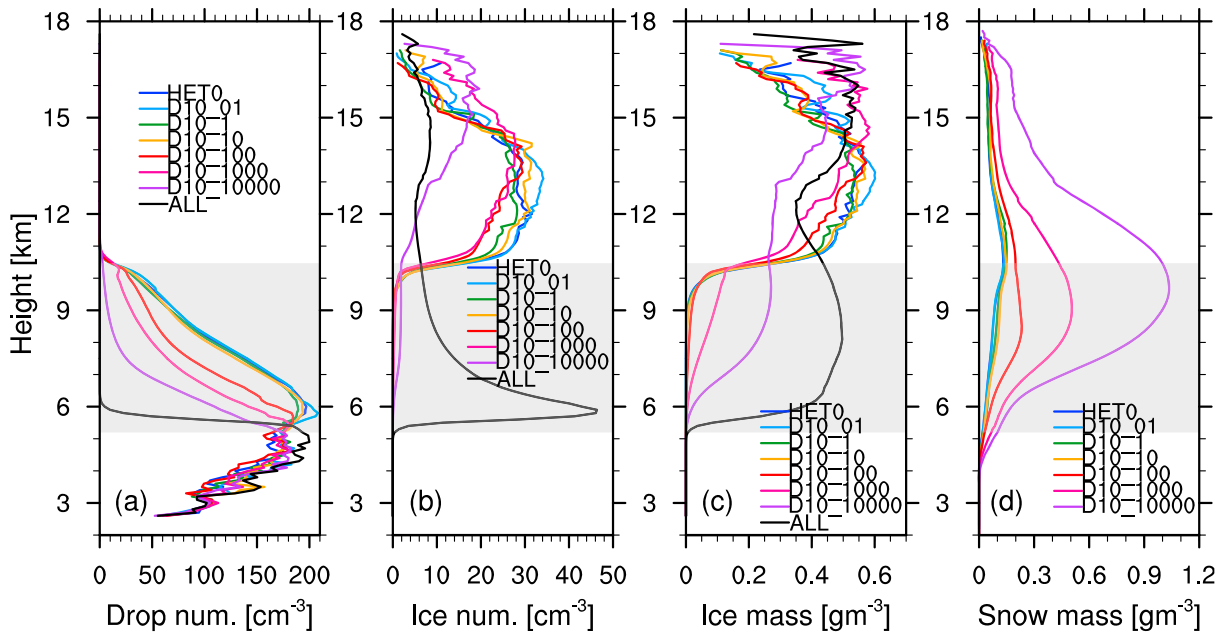
**Figure 10.** Same as Figure 6 but for the D10 runs.

crystal number concentration in anvils is reduced as HET is enhanced. These relationships are consistent with what is found in the BIGG runs.

The main differences between the BIGG runs and the D10 runs seem to stem from the altitudes at which HET is enhanced: according to Figure 4, the temperature dependence of HET is much stronger in the BIGG runs than that in the D10 runs. Although it is challenging to compare the BIGG runs and the D10 runs due to their different dependence on time and INPs (section 2.2), the D10 and D15 runs can be compared to each other. Figure 11 shows the estimated numbers of heterogeneously nucleated ice crystals in the D15 runs, in comparison to those in the D10 runs. This figure suggests that the temperature dependence of HET in the D15 runs is somewhat stronger than that in the D10 runs (i.e., less HET at warmer temperatures and more HET at colder temperatures). Likely because of this weaker HET at warm temperatures, the overall droplet depletion
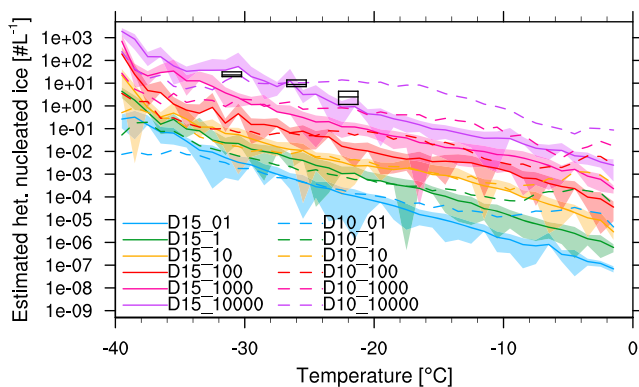


**Figure 11.** Heterogeneously nucleated ice number concentrations (L$^{-1}$) in the D15 runs averaged between 20 UTC on 22 June and 00 UTC on 23 June (10-min interval), along with their ± temporal standard deviation (shading; its lower half is not shown if its lower edge is a non-positive value). The same concentrations but in the D10 runs (presented in Figure 4) are shown by the dashed lines. These are estimated from the model output. As a reference, ground-based observational data of INPs from Table 1 of McCluskey et al. (2014) is shown with boxes.
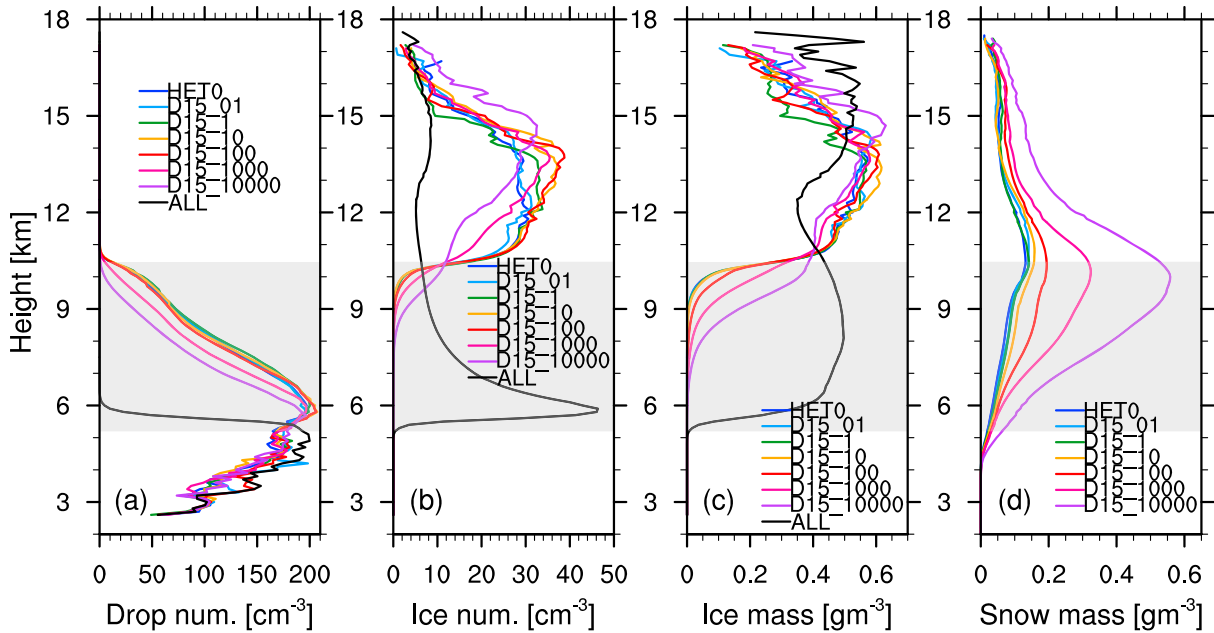
is weaker in the D15 runs (Figures 12a and 8c) than that in the D10 runs (Figures 10a and 8b). However, the stronger HET at cold temperatures in D15 can efficiently deplete droplets near the HOM level (Figure 12b) as in the BIGG runs (Figure 6b), and therefore, the overall microphysical response of the DCCs in D15 (Figures 7–9 and 12) is qualitatively the same as that in D10. This result indicates the robustness of the response of the DCCs to HET enhancements.

### 3.3. Impacts of Enhanced HET on the Radiative Properties of the DCCs

In this subsection, differences in the radiative properties of the DCCs among all the simulations are discussed. According to the previous subsections, ice crystal number concentrations above the HOM level change considerably with enhanced HET. This is confirmed by the vertical profiles of anvil ice crystal number concentrations shown in Figures 13a–13c. Furthermore, Figures 13d–13f show a reduction in ice mass concentrations in the anvils with enhanced HET. This can be explained by the enhanced snow production when HET is enhanced (e.g., Figure 6d). The numbers of grid boxes with either convective cores or anvils seem to be almost unaffected by the perturbations in HET (Figure 14). This insensitivity also applies to the horizontal coverage of anvil clouds (Figure 15); it should be noted that the differences in the *cumulative* counts of "anvil" grid boxes until 23 UTC

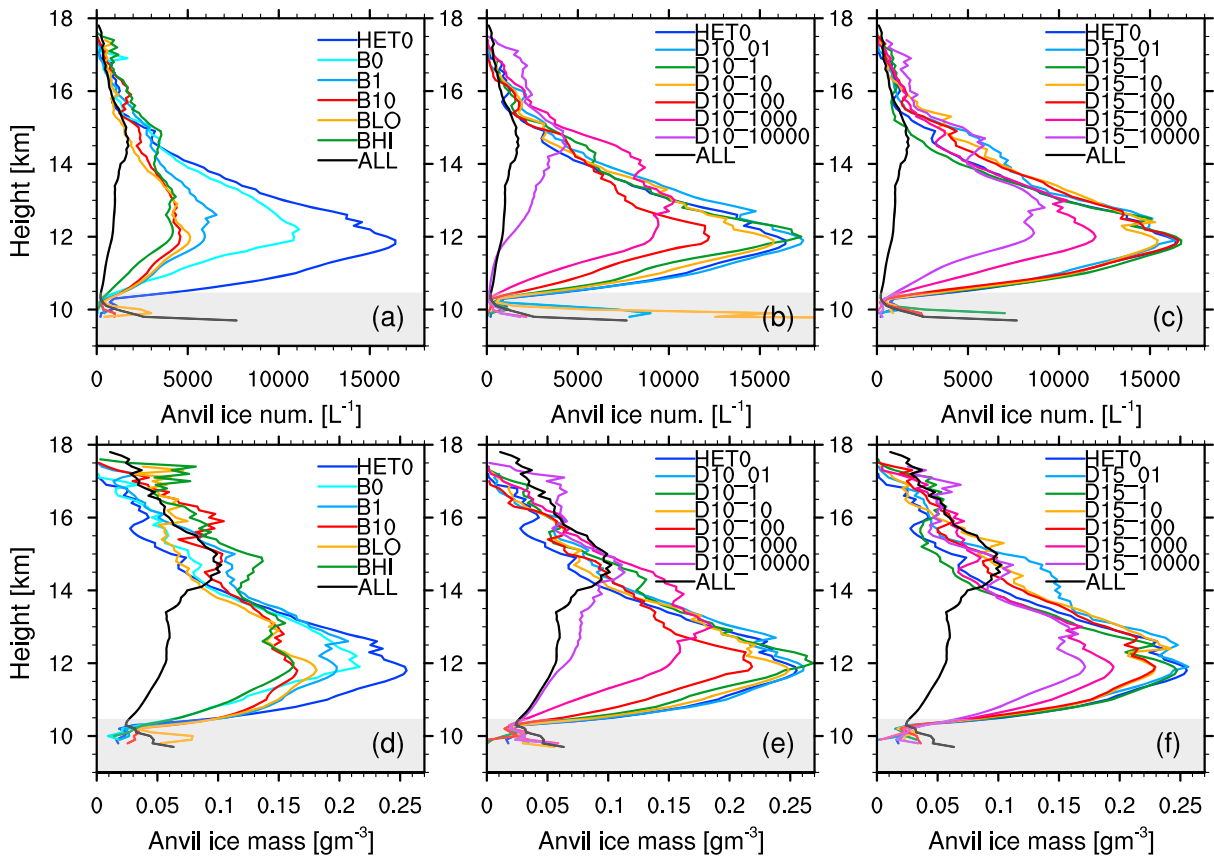**Figure 12.** Same as Figure 6 but for the D15 runs.



**Figure 13.** Vertical profiles of ice crystal (a–c) number (L$^{-1}$) and (d–f) mass (g/m$^3$) concentrations, both averaged inside "anvils" between 20 and 23 UTC on 22 June, in the (a and d) BIGG, (b and e) D10, and (c and f) D15 runs. The average altitudes of mixed-phase temperature range inside convective cores in HET0 are indicated by gray shading. These profiles are vertically interpolated at every 100 m.
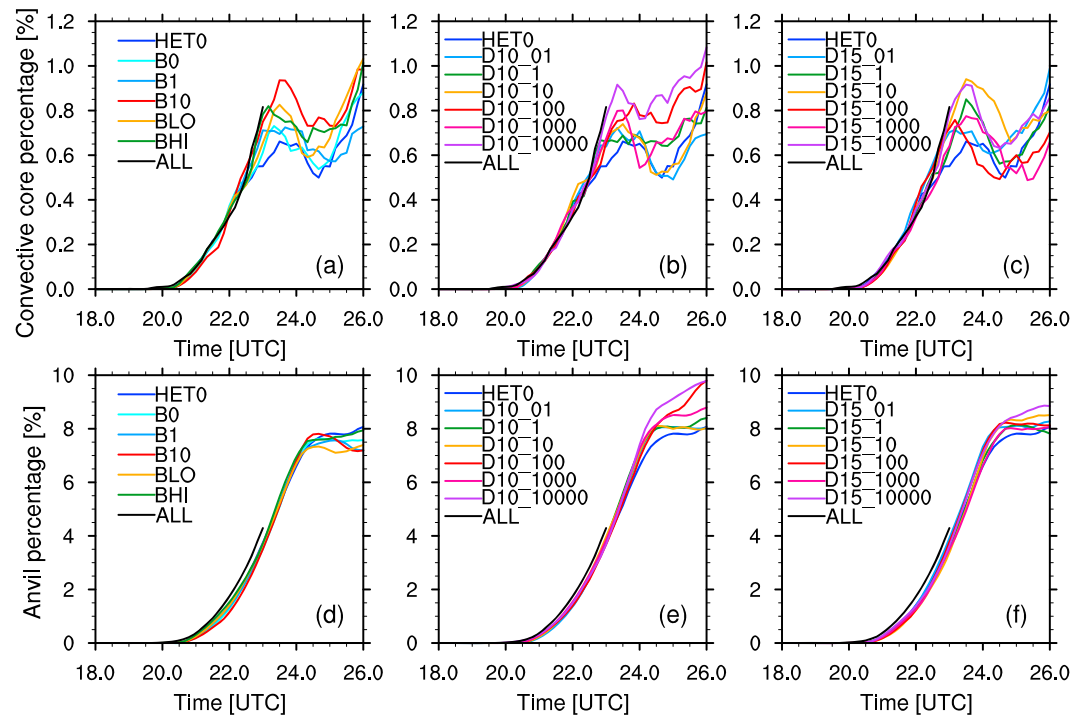
**Figure 14.** Temporal evolution of the percentages (%) of grid boxes in the inner domain (see Figure 1) that are categorized as (a–c) convective cores and (d–f) convective anvils in the (a and d) BIGG, (b and e) D10, and (c and f) D15 runs.
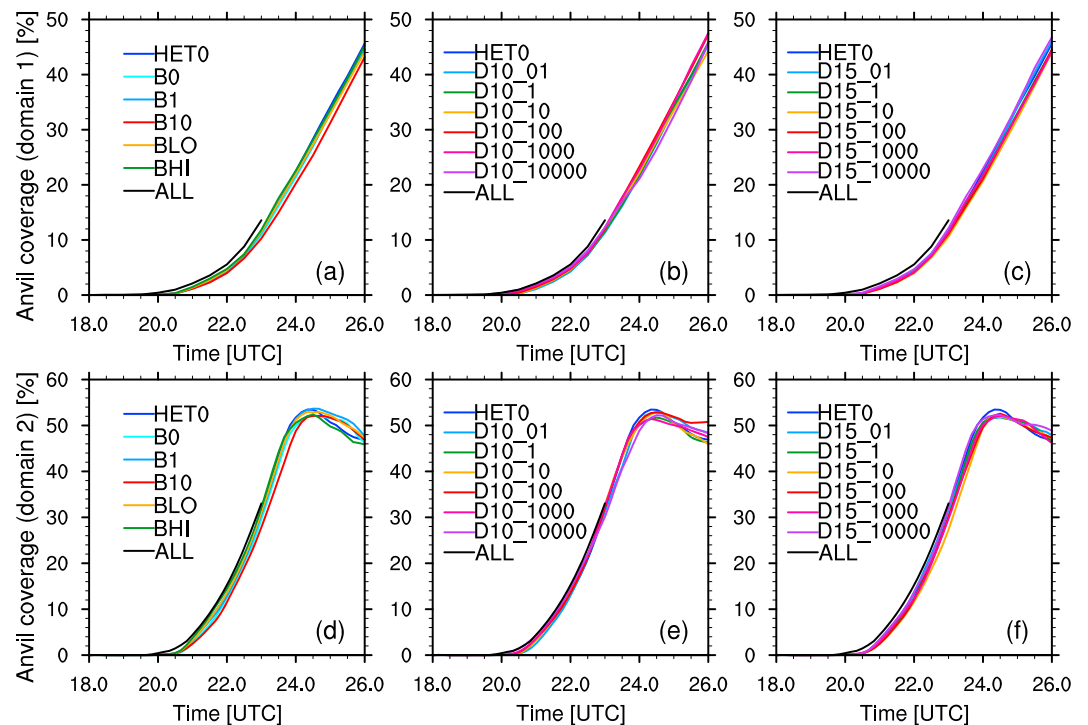


**Figure 15.** Temporal evolution of the percentages (%) of columns in the outer (a–c) and the inner (d–f) domains (see Figure 1) that contain convective anvils in the (a and d) BIGG, (b and e) D10, and the (c and f) D15 runs.
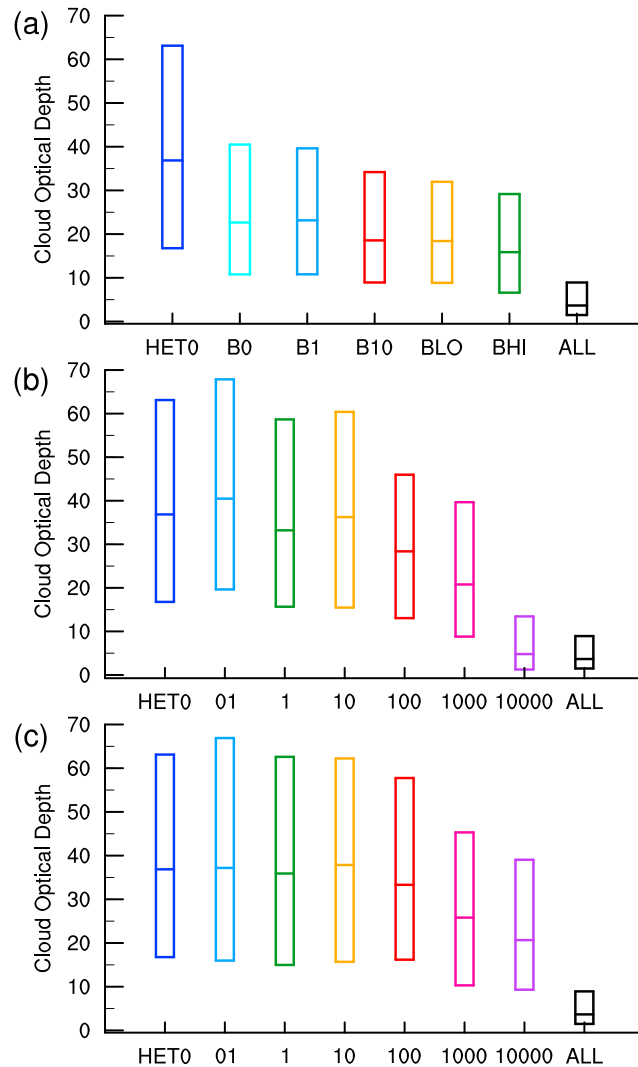
**Figure 16.** Box plots of estimated COD, from 20 to 23 UTC on 22 June (10-minute interval), in the (a) BIGG, (b) D10, and (c) D15 runs. The boxes show the upper and lower quartiles. Note that CODs are estimated from the model output (mass and number of hydrometeors) instead of directly output by the model. The calculation was done only for grid boxes of either convective cores or anvils, assuming droplet and ice size distributions described in Morrison et al. (2009). For (b) and (c), "D10_" and "D15_" are omitted from the x-axis labels, respectively.

in Figure 3b can be seen in Figure 15, but the differences are very small compared to the total numbers of "anvil" grid boxes that continue to grow after 23 UTC. From Figures 14 and 15, it is also evident that our simulation period and domains are not long and large enough, respectively, to fully capture the entire lifetime of the anvils.

In contrast, cloud optical depths (CODs) that are based on cloud droplet and cloud ice mass and number concentrations change significantly among the runs, as Figure 16 shows. It is clear from this figure that COD decreases as HET is enhanced. This reduction in COD can be explained by a reduction in ice mass, as shown in Figures 13d–13f and 17a–17c. In addition, an increase in ice crystal sizes with enhanced HET seems to also contribute to the decrease in COD, as Figures 17d–17f show. This is especially evident in the BIGG runs (Figure 17d) and not as clear in most of the D10/D15 runs (Figures 17e and 17f). There are several possible reasons for such a difference between the BIGG and D10/D15 runs; for instance, the strong HET at colder temperatures in BIGG (Figure 4) may efficiently deplete most of the droplets before HOM. It may be partly due to the differences in the way heterogeneously nucleated ice mass is calculated; the D10/D15 runs use a fixed ice crystal radius of 10 μm at the time of nucleation (section 2.2), whereas in the BIGG runs, it is parameterized as a function of droplet mass and numbers and also ambient conditions (e.g., temperature). While there are
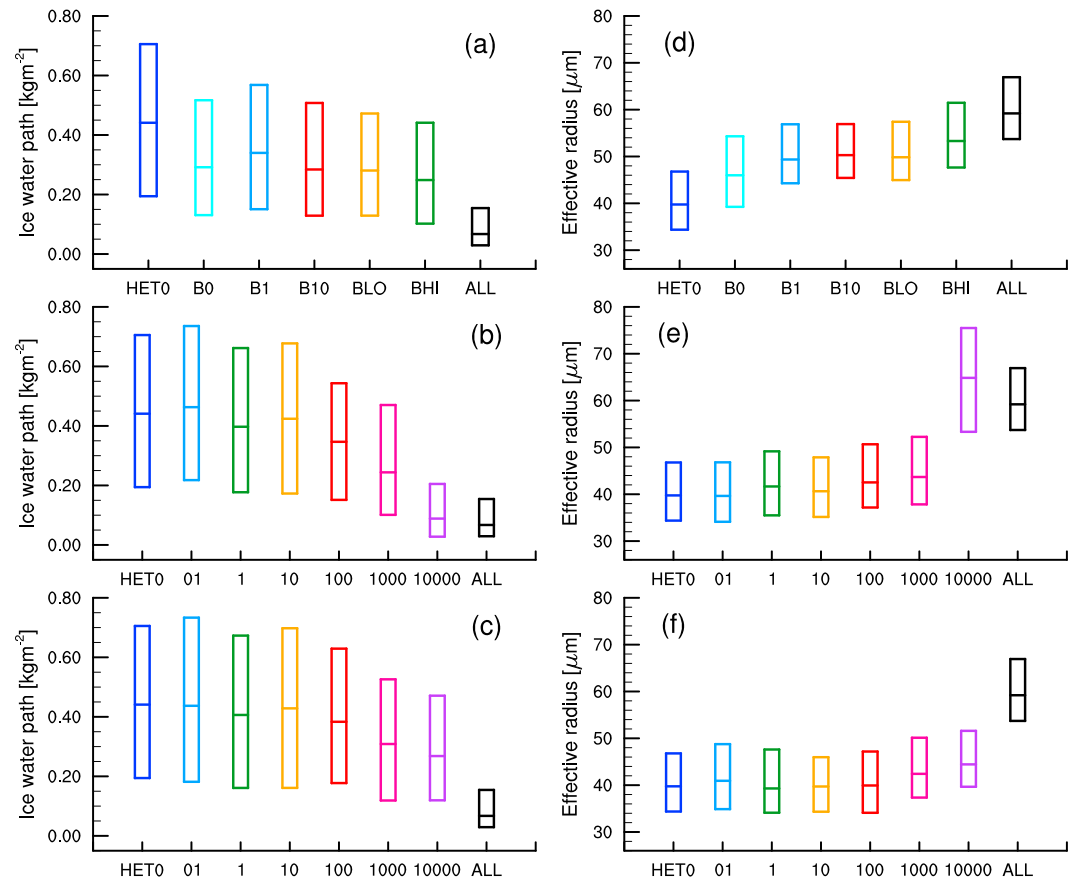
**Figure 17.** Same as Figure 16 but for (a–c) ice water path (kg/m$^2$) and (d–f) vertically averaged ice effective radius (μm) in the (a and d) BIGG, (b and e) D10, and (c and f) D15 runs.

slight differences in detailed mechanisms like this among the runs and their exact reason cannot be easily identified, we still find that an enhancement in HET generally leads to a decrease in the number and mass of ice crystals aloft, and also an increase in ice crystals sizes to varying extent, which all eventually reduce COD. As a result, the estimated cloud albedo ($\alpha_{cloud} = COD/(COD + 7)$, see Seinfeld and Pandis (1997) and Wood (2012)) also decreases with enhanced HET (Figure 18). The time series of mean cloud albedo in Figure 19 shows that its decreasing tendency with enhanced HET may potentially last for an extended period of time. Note that Figures 16–19 show either COD or cloud albedo and are hence based only on cloud droplets and ice crystals. The reason for showing COD or cloud albedo here, instead of total optical depth or total albedo (i.e., based on all hydrometeors), is to infer the varying radiative impacts of the DCCs on the global climate scale. On a local scale (e.g., our simulation domain), precipitating hydrometeors (i.e., snow, graupel, and rain) also contribute to optical depth (see Figure S7) and hence, there is not much difference in total albedo on a local scale among the simulations (Figure S8). However, this scale is too small/short to have significant impacts on climate. In order to estimate the long-term radiative impacts of DCCs on a larger scale from our regional simulations (which could not capture the entire life cycle of the DCCs), we investigate the cloud albedo based on cloud droplets and cloud ice, which typically remain much longer in the atmosphere and compose a significant part of convective anvils. The differences in microphysical and radiative properties between HET0-like and ALL-like DCCs are schematically depicted in Figure 20.

The microphysical differences among the simulations lead to dynamical differences, which are noticeable in Figure 18. It should be emphasized here that the differences among the simulations in this study may be due to both microphysical and dynamical differences, while both of them are initially triggered by the small microphysical perturbations. In order to fully separate the two impacts, state-of-the-art methods (such as the piggy-backing approach, Grabowski, 2015) need to be employed.
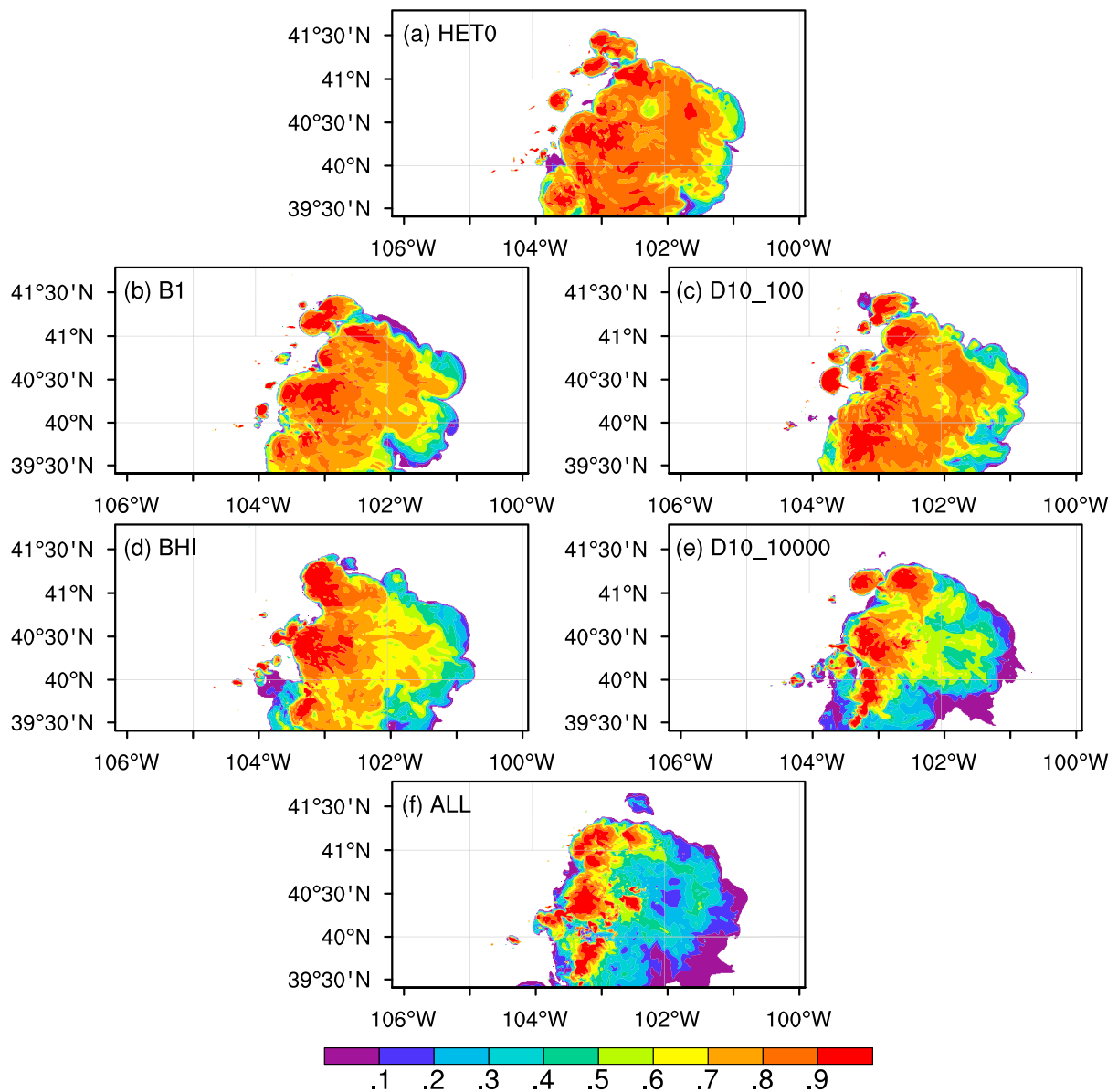
**Figure 18.** A top-down view of estimated cloud albedo at 23 UTC on 22 June, right before the ALL run terminates, in the (a) HET0, (b) B1, (c) D10_100, (d) BHI, (e) D10_10000, and (f) ALL runs. The calculation was done only for grid boxes of either convective cores or anvils and used model-output mass and number of hydrometeors, as in Figure 16.

## 4. Discussions

The following subsections discuss the applicability of the findings above (section 4.1) and the general implications for future studies of INP impacts on DCCs (section 4.2).

### 4.1. Relevance to Previous Studies

As introduced in section 1.1, the modeling studies by Ekman et al. (2007) and Fan et al. (2010b) have suggested invigoration of updrafts in DCCs as HET is enhanced, accompanied by an increase in anvil size. In our simulations, such an increase in updraft speed with enhanced HET exists, but is very small. Figure 21 shows vertical profiles of updraft speed averaged inside convective cores. A small increase in updraft speed due to enhanced freezing in the ALL run is seen between about 5 and 7 km, which is consistent with the altitudes of enhanced freezing shown in Figure 6b. The enhancement between about 10 and 14 km seems to be related to the number of "convective-core" grid boxes, since averaging is done over a fewer number of grid boxes that are closer to the center of the cores in ALL (Figures 3a and S1). An increase in updraft speed due to enhanced
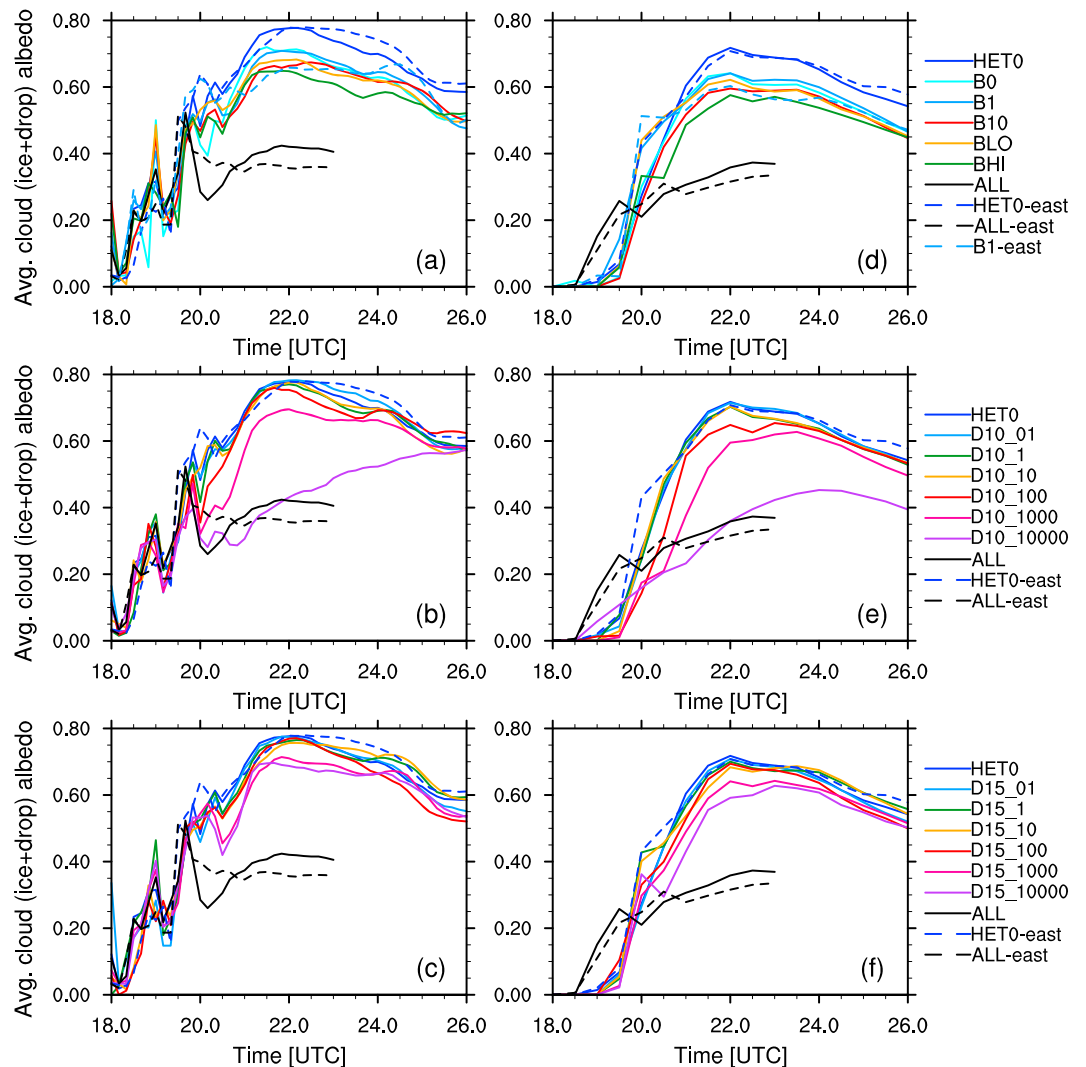
**Figure 19.** Time series of estimated cloud albedo averaged over (a–c) the inner domain and (d–f) the outer domain in the (a and d) BIGG, (b and e) D10, and (c and f) D15 runs. The calculation is done only over the columns in which either convective cores or anvils exist. This is estimated from the model output of hydrometeor mass and numbers, instead of directly output by the model. The results from the simulations with shifted domains (section 2.2) are shown by dashed lines ("-east"). Note that the ALL runs terminate around 23 UTC due to numerical instability (section 2.2).

freezing (5–7 km) is, therefore, small in our simulations. It is possible that this small change in updraft speed with enhanced HET is the reason for the unchanged anvil coverage in Figure 15.

We now discuss the potential reason why the inverse relationship between HET and HOM, as in Figure 7, is seen in our simulations but not necessarily in others. Such an inverse relationship, which can be thought of as the negative Twomey effect, is often applicable to cirrus clouds, and other clouds with weak vertical velocities where HET has large impacts (Eidhammer et al., 2009; Heymsfield et al., 2005). That is, the potential for a strong impact of HET is a necessary condition for the inverse relationship to be seen, and hence, clouds must form in conditions where either HET or HOM can dominate, depending on the INP availability. According to Eidhammer et al. (2009) (especially their Figure 4), however, the combination of strong updrafts and general scarcity of INPs seems to usually make HOM a dominant process inside DCCs, and this dominance cannot be easily perturbed by changes in INPs. Therefore, in a lot of DCCs, the inverse relationship cannot be seen as there is little room for HET to play a significant role. However, this view has been challenged by an observational study by Cziczo et al. (2013), which found a dominance of HET as a cirrus (including convective cirrus) formation mechanism. While updraft speed and INPs (or heterogeneously nucleated ice mass) seem to be the two most important factors in determining the dominance of HET and HOM (e.g., Eidhammer et al.,
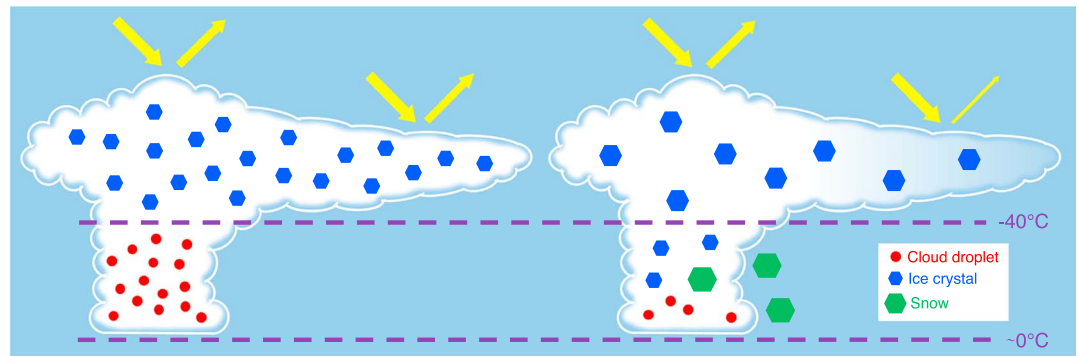
**Figure 20.** Relative characteristics of the DCCs found in this study, for the (left) HET0-like and (right) ALL-like DCCs. The optical depths of the clouds are similar between the two near the convective cores due to the contribution of precipitating hydrometeors (e.g., Figures S7 and S8) but may be different in the anvil part of the clouds as represented by different transparency of the clouds in this figure. Note that the size of ice crystals below the HOM level (relative to that above) depends on the case and is not discussed in this study.

2009), Heymsfield et al. (2005) (and their Figure 18 specifically) have suggested the importance of liquid water content as well: As liquid water content decreases, the dominance of HET may increase for the same updraft speed and preexisting ice water content, likely because the same amount of liquid depletion has more significant impacts on the total ice/liquid partitioning. In our simulations, the mean vertical velocities in convective cores (about 5–10 m/s, Figure 21) are high enough to have HOM-dominated DCCs where perturbations in HET should not play much of a role. However, liquid water content is very low as indicated by the high cloud base (at about 5 km and 0 °C, Figure 2), which enables varying HET to play a significant role in determining the anvil properties. As can be seen in Figure 22, most of the hydrometeor mass is frozen in the DCCs, and warm-rain processes by liquid hydrometeors seem to play a very small role. Therefore, the inverse relationship between HET and HOM in DCCs with strong updrafts may be seen if low liquid water content allows for the transition of
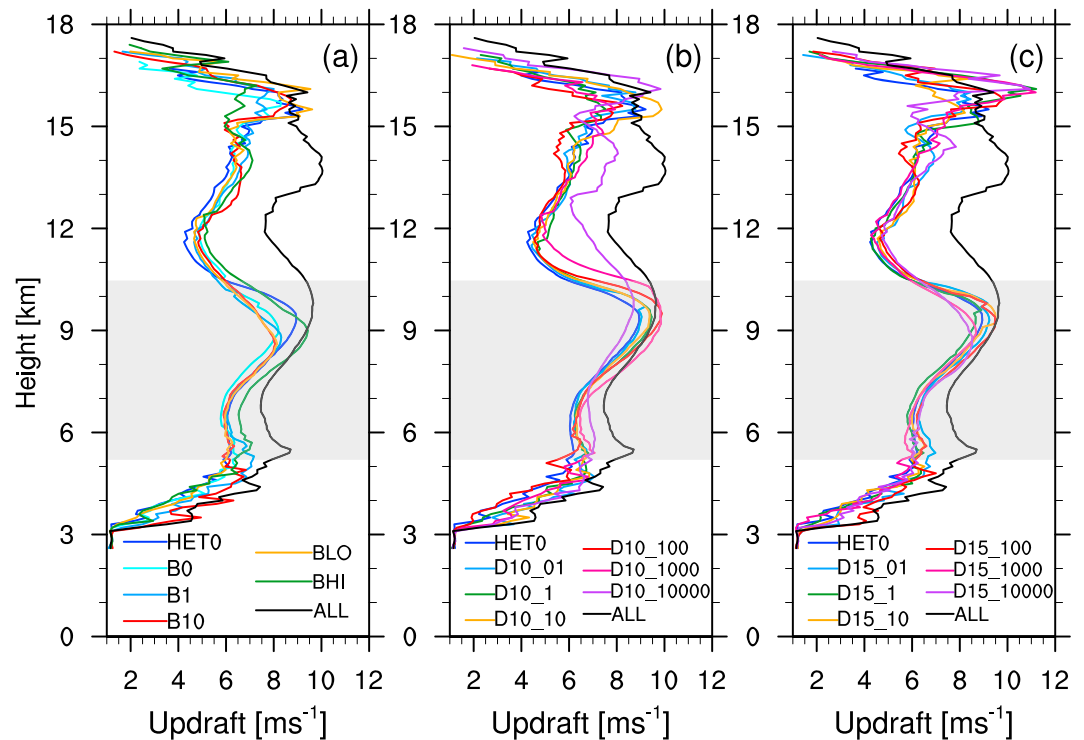


**Figure 21.** Mean updraft speed (m/s) inside convective cores in the (a) BIGG, (b) D10, and (c) D15 runs, averaged between 20 UTC and 23 UTC on 22 June (10-min interval). The average altitudes of mixed-phase temperature range inside convective cores in HET0 are indicated by gray shading. These profiles are vertically interpolated at every 100 m.
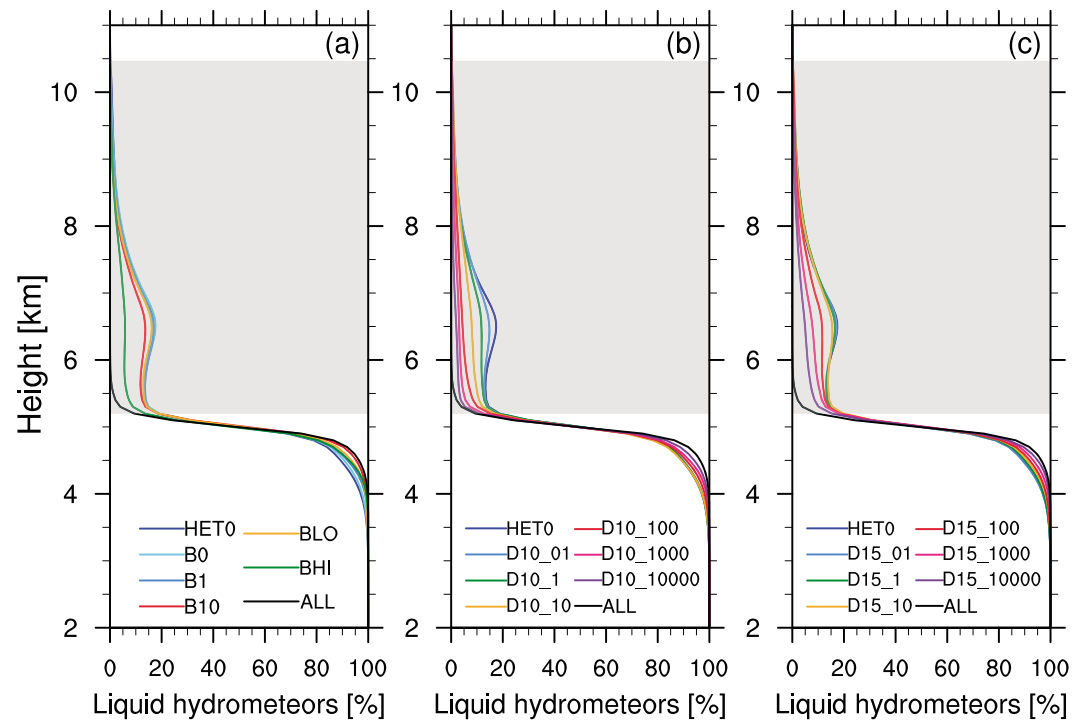
**Figure 22.** Mean percentages (%) of liquid hydrometeor masses (liquid droplets and rain) in total hydrometeor masses (liquid droplets, rain, ice crystals, snow, and graupel) in the (a) BIGG, (b) D10, and (c) D15 runs, averaged between 20 UTC and 23 UTC on 22 June (10-min interval). These are calculated only in grid boxes with nonzero liquid/solid hydrometeor mass. The average altitudes of mixed-phase temperature range inside convective cores in HET0 are indicated by gray shading. These profiles are vertically interpolated at every 100 m.

the dominance between HET and HOM. A low cloud-base height (i.e., warm cloud-base temperature) in Fan et al. (2010b) (see their Figure 2), for example, suggests a larger liquid water content, and hence, its complete depletion by HET may be unlikely. Instead, varying HET may modify latent heat release during freezing quite significantly, unlike our simulations, owing to the large liquid water content. This is qualitatively in agreement with a finding in Storer et al. (2010) that clouds developing with weaker CAPE (e.g., drier low level) may be subject to more significant aerosol effects.

### 4.2. Implications

The cold cloud base in our simulations may be common in the region of our simulations (Figure 1), according to generally low dew point temperatures in the western half of the United States (see Figure 1 in Rosenfeld & Bell, 2011). Our findings may be applicable to convective clouds in the western United States and similar environments, as well as DCCs with limited liquid availability. If aerosol perturbations by the projected increase in wildfires in the western United States predominantly lead to increased CCN concentrations, for example, convective anvil clouds may have more ice crystals, depending on the dominance of HET and HOM. On the other hand, if aerosol perturbations include significant contributions of INPs that greatly enhance HET, the anvils may have fewer ice crystals. We would like to emphasize the importance of liquid water content in determining the dominance of HET and HOM, as has been indicated in Figure 18 of Heymsfield et al. (2005) for DCCs and in Figure 1 of Kärcher (2017) for cirrus clouds. The dominance of HET or HOM matters significantly when aerosol impacts on clouds are considered, while the relative importance of HET and HOM may also itself be impacted by aerosols (i.e., INPs) to some extent.

## 5. Conclusions

The sensitivity tests of enhanced HET in cloud-resolving WRF-CHEM simulations have revealed the following features of the simulated DCCs:

1. Enhanced HET generally results in reduced ice crystal number concentrations in the anvils, likely due to enhanced depletion of liquid droplets by ice and snow growth (Figures 7 and 8).

2. The HET enhancements at warm temperatures (low altitudes) are more efficient in depleting liquid droplets than those at cold temperatures (high altitudes), according to the comparison of the BHI run and the BLO run. This indicates the importance of the *types/properties* of INPs (i.e., active at different temperatures), in addition to their amounts, in determining their impacts on DCCs. This needs to be taken into consideration when aerosol-cloud interactions are investigated.

3. COD and cloud albedo that are based on cloud droplets and cloud ice generally decrease with enhanced HET. This is partly due to the decreased mass of ice aloft (Figures 13d–13f). In the BIGG runs and the ALL run, increased ice crystal sizes also contribute to the reduced COD and cloud albedo (Figure 17).

4. The results of this study suggest that cloud-base temperature (or liquid water content) is crucial in determining the relative dominance of HET and HOM in DCCs, in addition to updraft speed and INP availability as suggested by previous studies.

5. An inverse relationship between HET and HOM, which may be typically applicable to high cirrus clouds, is seen in our simulations of DCCs. We speculate that the conditions for the simulated DCCs, such as the cold cloud-base temperature and the limited availability of liquid water, led to the indirect competition between HET and HOM for cloud droplets. Our findings, therefore, may be applicable to DCCs with cold cloud-base temperatures that are more prevalent in the western United States and other dry and/or elevated regions.

On the other hand, the following points are beyond the scope of this study and need further investigation in the near future:

1. Understanding exactly how the dominance of HET and HOM is determined by vertical velocities, INP availability, and liquid water content requires further analyses of numerous DCCs both in model simulations and in observational data sets.

2. Sensitivities of convective anvils to varying droplet concentrations seem to depend on the relative dominance of HET and HOM, but the detailed dependence was not explored in this study.

3. Changes in the impacts of DCCs on climate through their radiative properties were not rigorously analyzed in this study.

4. For the complete isolation of microphysical impacts from dynamical impacts, simulations with the piggybacking approach (e.g., Grabowski, 2015) are necessary.

While ice microphysical processes in DCCs still remain poorly understood, the results of this study suggest a strong dependence of aerosol effects on the relative dominance of HET and HOM, which in turn may be controlled by INP availability. Overall, understanding the ability of aerosol particles to serve as INPs emerges as a crucial theme for disentangling aerosol-cloud interactions that include ice microphysical processes.

## References

Achakulwisut, P., Shen, L., & Mickley, L. J. (2017). What controls springtime fine dust variability in the western United States? Investigating the 2002-2015 increase in fine dust in the U.S Southwest. *Journal of Geophysical Research: Atmospheres*, *122*, 12,449–12,467. https://doi.org/10.1002/2017JD027208

Ackermann, I. J., Hass, H., Memmesheimer, M., Ebel, A., Binkowski, F. S., & Shankar, U. (1998). Modal aerosol dynamics model for Europe: Development and first applications. *Atmospheric Environment*, *32*(17), 2981–2999. https://doi.org/10.1016/S1352-2310(98)00006-5

Altaratz, O., Koren, I., Remer, L. A., & Hirsch, E. (2014). Review: Cloud invigoration by aerosols — Coupling between microphysics and dynamics. *Atmospheric Research*, *140-141*, 38–60. https://doi.org/10.1016/j.atmosres.2014.01.009

Barth, M. C., Cantrell, C. A., Brune, W. H., Rutledge, S. A., Crawford, J. H., Huntrieser, H., et al. (2015). The Deep Convective Clouds and Chemistry (DC3) field campaign. *Bulletin of the American Meteorological Society*, *96*(8), 1281–1309. https://doi.org/10.1175/BAMS-D-13-00290.1

Beljaars, A. C. M. (1995). The parametrization of surface fluxes in large-scale models under free convection. *Quarterly Journal of the Royal Meteorological Society*, *121*(522), 255–270. https://doi.org/10.1002/qj.49712152203

Bigg, E. K. (1953). The formation of atmospheric ice crystals by the freezing of droplets. *Quarterly Journal of the Royal Meteorological Society*, *79*(342), 510–519. https://doi.org/10.1002/qj.49707934207

Bretherton, C. S., & Park, S. (2009). A new moist turbulence parameterization in the community atmosphere model. *Journal of Climate*, *22*(12), 3422–3448. https://doi.org/10.1175/2008JCLI2556.1

Carrió, G. G., van den Heever, S. C., & Cotton, W. R. (2007). Impacts of nucleating aerosol on anvil-cirrus clouds: A modeling study. *Atmospheric Research*, *84*(2), 111–131. https://doi.org/10.1016/j.atmosres.2006.06.002

Chen, G, NASA Langley Research Center (LaRC), & Olson, J. R. (2014). NASA DC-8 1 Second Data Merge. Version 2.0, UCAR/NCAR - Earth Observing Laboratory, https://doi.org/10.5065/D6SF2TXB

Cziczo, D. J., Froyd, K. D., Hoose, C., Jensen, E. J., Diao, M., Zondlo, M. A., et al. (2013). Clarifying the dominant sources and mechanisms of cirrus cloud formation. *Science*, *340*(6138), 1320–1324. https://doi.org/10.1126/science.1234145

DeMott, P. J. (1990). An exploratory study of ice nucleation by soot aerosols. *Journal of Applied Meteorology*, *29*(10), 1072–1079. https://doi.org/10.1175/1520-0450(1990)029<1072:AESOIN>2.0.CO;2

DeMott, P. J., Chen, Y., Kreidenweis, S. M., Rogers, D. C., & Sherman, D. E. (1999). Ice formation by black carbon particles. *Geophysical Research Letters*, *26*(16), 2429–2432. https://doi.org/10.1029/1999GL900580

DeMott, P. J., Hill, T. C. J., McCluskey, C. S., Prather, K. A., Collins, D. B., Sullivan, R. C., et al. (2016). Sea spray aerosol as a unique source of ice nucleating particles. *Proceedings of the National Academy of Sciences*, *113*(21), 5797–5803. https://doi.org/10.1073/pnas.1514034112

DeMott, P. J., Prenni, A. J., Liu, X., Kreidenweis, S. M., Petters, M. D., Twohy, C. H., et al. (2010). Predicting global atmospheric ice nuclei distributions and their impacts on climate. *Proceedings of the National Academy of Sciences*, *107*(25), 11,217–11,222. https://doi.org/10.1073/pnas.0910818107

DeMott, P. J., Prenni, A. J., McMeeking, G. R., Sullivan, R. C., Petters, M. D., Tobo, Y., et al. (2015). Integrating laboratory and field data to quantify the immersion freezing ice nucleation activity of mineral dust particles. *Atmospheric Chemistry and Physics*, *15*(1), 393–409. https://doi.org/10.5194/acp-15-393-2015

DeMott, P. J., Sassen, K., Poellot, M. R., Baumgardner, D., Rogers, D. C., Brooks, S. D., et al. (2003). African dust aerosols as atmospheric ice nuclei. *Geophysical Research Letters*, *30*(14), 1732. https://doi.org/10.1029/2003GL017410

Dennison, P. E., Brewer, S. C., Arnold, J. D., & Moritz, M. A. (2014). Large wildfire trends in the western United States, 1984–2011. *Geophysical Research Letters*, *41*, 2928–2933. https://doi.org/10.1002/2014GL059576

Diehl, K., & Mitra, S. K. (2015). New particle-dependent parameterizations of heterogeneous freezing processes: Sensitivity studies of convective clouds with an air parcel model. *Atmospheric Chemistry and Physics*, *15*(22), 12,741–12,763. https://doi.org/10.5194/acp-15-12741-2015

Dyer, A. J., & Hicks, B. B. (1970). Flux-gradient relationships in the constant flux layer. *Quarterly Journal of the Royal Meteorological Society*, *96*(410), 715–721. https://doi.org/10.1002/qj.49709641012

Eidhammer, T., DeMott, P. J., & Kreidenweis, S. M. (2009). A comparison of heterogeneous ice nucleation parameterizations using a parcel model framework. *Journal of Geophysical Research*, *114*, D06202. https://doi.org/10.1029/2008JD011095

Ekman, A. M. L., Engström, A., & Wang, C. (2007). The effect of aerosol composition and concentration on the development and anvil properties of a continental deep convective cloud. *Quarterly Journal of the Royal Meteorological Society*, *133*(627), 1439–1452. https://doi.org/10.1002/qj.108

Fan, J., Comstock, J. M., & Ovchinnikov, M. (2010a). The cloud condensation nuclei and ice nuclei effects on tropical anvil characteristics and water vapor of the tropical tropopause layer. *Environmental Research Letters*, *5*(4), 044005. https://doi.org/10.1088/1748-9326/5/4/044005

Fan, J., Comstock, J. M., Ovchinnikov, M., McFarlane, S. A., McFarquhar, G., & Allen, G. (2010b). Tropical anvil characteristics and water vapor of the tropical tropopause layer: Impact of heterogeneous and homogeneous freezing parameterizations. *Journal of Geophysical Research*, *115*, D12201. https://doi.org/10.1029/2009JD012696

Fan, J., Wang, Y., Rosenfeld, D., & Liu, X. (2016). Review of aerosol–cloud interactions: Mechanisms, significance, and challenges. *Journal of the Atmospheric Sciences*, *73*(11), 4221–4252. https://doi.org/10.1175/JAS-D-16-0037.1

Field, P. R., Lawson, R. P., Brown, P. R. A., Lloyd, G., Westbrook, C., Moisseev, D., et al. (2017). Secondary ice production: Current state of the science and recommendations for the future. *Meteorological Monographs*, *58*, 7.1–7.20. https://doi.org/10.1175/AMSMONOGRAPHS-D-16-0014.1

Freitas, S. R., Longo, K. M., Alonso, M. F., Pirre, M., Marecal, V., Grell, G., et al. (2011). PREP-CHEM-SRC–1.0: A preprocessor of trace gas and aerosol emission fields for regional and global atmospheric chemistry models. *Geoscientific Model Development*, *4*(2), 419–433. https://doi.org/10.5194/gmd-4-419-2011

Giangrande, S. E., Toto, T., Jensen, M. P., Bartholomew, M. J., Feng, Z., Protat, A., et al. (2016). Convective cloud vertical velocity and mass-flux characteristics from radar wind profiler observations during GoAmazon2014/5. *Journal of Geophysical Research: Atmospheres*, *121*, 12,891–12,913. https://doi.org/10.1002/2016JD025303

Grabowski, W. W. (2015). Untangling microphysical impacts on deep convection applying a novel modeling methodology. *Journal of the Atmospheric Sciences*, *72*(6), 2446–2464. https://doi.org/10.1175/JAS-D-14-0307.1

Grabowski, W. W., & Morrison, H. (2016). Untangling microphysical impacts on deep convection applying a novel modeling methodology. Part II: Double-moment microphysics. *Journal of the Atmospheric Sciences*, *73*(9), 3749–3770. https://doi.org/10.1175/JAS-D-15-0367.1

Grabowski, W. W., & Morrison, H. (2017). Modeling condensation in deep convection. *Journal of the Atmospheric Sciences*, *74*(7), 2247–2267. https://doi.org/10.1175/JAS-D-16-0255.1

Grell, G. A., Peckham, S. E., Schmitz, R., McKeen, S. A., Frost, G., Skamarock, W. C., & Eder, B. (2005). Fully coupled "online" chemistry within the WRF model. *Atmospheric Environment*, *39*(37), 6957–6975. https://doi.org/10.1016/j.atmosenv.2005.04.027

Guenther, A., Karl, T., Harley, P., Wiedinmyer, C., Palmer, P. I., & Geron, C. (2006). Estimates of global terrestrial isoprene emissions using MEGAN (Model of Emissions of Gases and Aerosols from Nature). *Atmospheric Chemistry and Physics*, *6*(11), 3181–3210. https://doi.org/10.5194/acp-6-3181-2006

Hallar, A. G., Petersen, R., Andrews, E., Michalsky, J., McCubbin, I. B., & Ogren, J. A. (2015). Contributions of dust and biomass burning to aerosols at a Colorado mountain-top site. *Atmospheric Chemistry and Physics*, *15*(23), 13,665–13,679. https://doi.org/10.5194/acp-15-13665-2015

Hess, M., Koepke, P., & Schult, I. (1998). Optical properties of aerosols and clouds: The software package OPAC. *Bulletin of the American Meteorological Society*, *79*(5), 831–844. https://doi.org/10.1175/1520-0477(1998)079<0831:OPOAAC>2.0.CO;2

Heymsfield, A. J., Miloshevich, L. M., Schmitt, C., Bansemer, A., Twohy, C., Poellot, M. R., et al. (2005). Homogeneous ice nucleation in subtropical and tropical convection and its influence on cirrus anvil microphysics. *Journal of the Atmospheric Sciences*, *62*(1), 41–64. https://doi.org/10.1175/JAS-3360.1

Hiron, T., & Flossmann, A. I. (2015). A study of the role of the parameterization of heterogeneous ice nucleation for the modeling of microphysics and precipitation of a convective cloud. *Journal of the Atmospheric Sciences*, *72*(9), 3322–3339. https://doi.org/10.1175/JAS-D-15-0026.1

Hobbs, P. V., & Locatelli, J. D. (1969). Ice nuclei from a natural forest fire. *Journal of Applied Meteorology*, *8*(5), 833–834. https://doi.org/10.1175/1520-0450(1969)008<0833:INFANF>2.0.CO;2

Iacono, M. J., Delamere, J. S., Mlawer, E. J., Shephard, M. W., Clough, S. A., & Collins, W. D. (2008). Radiative forcing by long-lived greenhouse gases: Calculations with the AER radiative transfer models. *Journal of Geophysical Research*, *113*, D13103. https://doi.org/10.1029/2008JD009944

Jensen, E., Starr, D., & Toon, O. B. (2004). Mission investigates tropical cirrus clouds. *EOS Transactions American Geophysical Union*, *85*(5), 45–50, https://doi.org/10.1029/2004EO050002

Jolly, W. M., Cochrane, M. A., Freeborn, P. H., Holden, Z. A., Brown, T. J., Williamson, G. J., & Bowman, D. M. J. S. (2015). Climate-induced variations in global wildfire danger from 1979 to 2013. *Nature Communications*, *6*, 7537. https://doi.org/10.1038/ncomms8537

Kanji, Z. A., Ladino, L. A., Wex, H., Boose, Y., Burkert-Kohn, M., Cziczo, D. J., & Krämer, M. (2017). Overview of ice nucleating particles. *Meteorological Monographs*, *58*, 1.1–1.33. https://doi.org/10.1175/AMSMONOGRAPHS-D-16-0006.1

Kärcher, B. (2017). Cirrus clouds and their response to anthropogenic activities. *Current Climate Change Reports*, *3*(1), 45–57. https://doi.org/10.1007/s40641-017-0060-3

**AGU**
100
ADVANCING EARTH
AND SPACE SCIENCE

**Journal of Geophysical Research: Atmospheres**

10.1029/2018JD028889

Kärcher, B., Hendricks, J., & Lohmann, U. (2006). Physically based parameterization of cirrus cloud formation for use in global atmospheric models. *Journal of Geophysical Research*, *111*, D01205. https://doi.org/10.1029/2005JD006219

Kärcher, B., & Lohmann, U. (2003). A parameterization of cirrus cloud formation: Heterogeneous freezing. *Journal of Geophysical Research*, *108*(D14), 4402. https://doi.org/10.1029/2002JD003220

Khain, A. P., BenMoshe, N., & Pokrovsky, A. (2008). Factors determining the impact of aerosols on surface precipitation from clouds: An attempt at classification. *Journal of the Atmospheric Sciences*, *65*(6), 1721–1748. https://doi.org/10.1175/2007JAS2515.1

Khain, A., Ovtchinnikov, M., Pinsky, M., Pokrovsky, A., & Krugliak, H. (2000). Notes on the state-of-the-art numerical modeling of cloud microphysics. *Atmospheric Research*, *55*(3), 159–224. https://doi.org/10.1016/S0169-8095(00)00064-8

Lawson, P. (2014). NASA DC-8 2-DS Data. Version 1.0, UCAR/NCAR - Earth Observing Laboratory, https://doi.org/10.5065/D6NP235Z

Lawson, R. P., O'Connor, D., Zmarzly, P., Weaver, K., Baker, B., Mo, Q., & Jonsson, H. (2006). The 2D-S (Stereo) Probe: Design and preliminary tests of a new airborne, high-speed, high-resolution particle imaging probe. *Journal of Atmospheric and Oceanic Technology*, *23*(11), 1462–1477. https://doi.org/10.1175/JTECH1927.1

Liu, Y., Goodrick, S. L., & Stanturf, J. A. (2013). Future U.S. wildfire potential trends projected using a dynamically downscaled climate change scenario. *Forest Ecology and Management*, *294*, 120–135. https://doi.org/10.1016/j.foreco.2012.06.049

McCluskey, C. S., DeMott, P. J., Prenni, A. J., Levin, E. J. T., McMeeking, G. R., Sullivan, A. P., et al. (2014). Characteristics of atmospheric ice nucleating particles associated with biomass burning in the US: Prescribed burns and wildfires. *Journal of Geophysical Research: Atmospheres*, *119*, 10,458–10,470. https://doi.org/10.1002/2014JD021980

Mitchell, D. L., & Finnegan, W. (2009). Modification of cirrus clouds to reduce global warming. *Environmental Research Letters*, *4*(4), 045102. https://doi.org/10.1088/1748-9326/4/4/045102

Morrison, H., Thompson, G., & Tatarskii, V. (2009). Impact of cloud microphysics on the development of trailing stratiform precipitation in a simulated squall line: Comparison of one- and two-moment schemes. *Monthly Weather Review*, *137*(3), 991–1007. https://doi.org/10.1175/2008MWR2556.1

Paulson, C. A. (1970). The mathematical representation of wind speed and temperature profiles in the unstable atmospheric surface layer. *Journal of Applied Meteorology*, *9*(6), 857–861. https://doi.org/10.1175/1520-0450(1970)009<0857:TMROWS>2.0.CO;2

Petters, M. D., Parsons, M. T., Prenni, A. J., DeMott, P. J., Kreidenweis, S. M., Carrico, C. M., et al. (2009). Ice nuclei emissions from biomass burning. *Journal of Geophysical Research*, *114*, D07209. https://doi.org/10.1029/2008JD011532

Phillips, V. T. J., Donner, L. J., & Garner, S. T. (2007). Nucleation processes in deep convection simulated by a cloud-system-resolving model with double-moment bulk microphysics. *Journal of the Atmospheric Sciences*, *64*(3), 738–761. https://doi.org/10.1175/JAS3869.1

Prenni, A. J., DeMott, P. J., Sullivan, A. P., Sullivan, R. C., Kreidenweis, S. M., & Rogers, D. C. (2012). Biomass burning as a potential source for atmospheric ice nuclei: Western wildfires and prescribed burns. *Geophysical Research Letters*, *39*, L11805. https://doi.org/10.1029/2012GL051915

Reisin, T., Tzivion, S., & Levin, Z. (1996). Seeding convective clouds with ice nuclei or hygroscopic particles: A numerical study using a model with detailed microphysics. *Journal of Applied Meteorology*, *35*(9), 1416–1434. https://doi.org/10.1175/1520-0450(1996)035<1416:SCCWIN>2.0.CO;2

Rippey, B. R. (2015). The U.S. drought of 2012. *Weather and Climate Extremes*, *10*(Part A), 57–64. https://doi.org/10.1016/j.wace.2015.10.004

Rosenfeld, D., Andreae, M. O., Asmi, A., Chin, M., Leeuw, G., Donovan, D. P., et al. (2014). Global observations of aerosol-cloud-precipitation-climate interactions. *Reviews of Geophysics*, *52*, 750–808. https://doi.org/10.1002/2013RG000441

Rosenfeld, D., & Bell, T. L. (2011). Why do tornados and hailstorms rest on weekends? *Journal of Geophysical Research*, *116*, D20211. https://doi.org/10.1029/2011JD016214

Rosenfeld, D., Lohmann, U., Raga, G. B., O'Dowd, C. D., Kulmala, M., Fuzzi, S., et al. (2008). Flood or drought: How do aerosols affect precipitation? *Science*, *321*(5894), 1309–1313. https://doi.org/10.1126/science.1160606

Rosenfeld, D., & Woodley, W. L. (2000). Deep convective clouds with sustained supercooled liquid water down to -37.5°C. *Nature*, *405*, 440–442. https://doi.org/10.1038/35013030

Sassen, K., & Khvorostyanov, V. I. (2008). Cloud effects from boreal forest fire smoke: Evidence for ice nucleation from polarization lidar data and cloud model simulations. *Environmental Research Letters*, *3*(2), 025006. https://doi.org/10.1088/1748-9326/3/2/025006

Schell, B., Ackermann, I. J., Hass, H., Binkowski, F. S., & Ebel, A. (2001). Modeling the formation of secondary organic aerosol within a comprehensive air quality model system. *Journal of Geophysical Research*, *106*(D22), 28,275–28,293. https://doi.org/10.1029/2001JD000384

Schultz, M. G., Heil, A., Hoelzemann, J. J., Spessa, A., Thonicke, K., Goldammer, J. G., et al. (2008). Global wildland fire emissions from 1960 to 2000. *Global Biogeochemical Cycles*, *22*, GB2002. https://doi.org/10.1029/2007GB003031

Seinfeld, J. H., & Pandis, S. N. (1997). *Atmospheric Chemistry and Physics: From Air Pollution to Climate Change*. New York: Wiley-Interscience.

Skamarock, W. C., Klemp, J. B., Dudhia, J., Gill, D. O., Barker, D. M., Duda, M. G., et al. (2008). A Description of the Advanced Research WRF Version 3, NCAR Technical Note, NCAR/TN-475+STR.

Stockwell, W. R., Middleton, P., Chang, J. S., & Tang, X. (1990). The second generation regional acid deposition model chemical mechanism for regional air quality modeling. *Journal of Geophysical Research*, *95*(D10), 16,343–16,367. https://doi.org/10.1029/JD095iD10p16343

Storer, R. L., van den Heever, S. C., & Stephens, G. L. (2010). Modeling aerosol impacts on convective storms in different environments. *Journal of the Atmospheric Sciences*, *67*(12), 3904–3915. https://doi.org/10.1175/2010JAS3363.1

Tao, W.-K., Chen, J.-P., Li, Z., Wang, C., & Zhang, C. (2012). Impact of aerosols on convective clouds and precipitation. *Reviews of Geophysics*, *50*, RG2001. https://doi.org/10.1029/2011RG000369

Teller, A., & Levin, Z. (2006). The effects of aerosols on precipitation and dimensions of subtropical clouds: A sensitivity study using a numerical cloud model. *Atmospheric Chemistry and Physics*, *6*(1), 67–80. https://doi.org/10.5194/acp-6-67-2006

Tewari, M., Chen, F., Wang, W., Dudhia, J., LeMone, M. A., Mitchell, K., et al. (2004). Implementation and verification of the unified NOAH land surface model in the WRF model. In *20th conference on weather analysis and forecasting/16th conference on numerical weather prediction*, pp. 11–15.

UCAR/NCAR (Earth Observing Laboratory) (2013). EOL MISS Colorado Sounding Data. Version 1.0, UCAR/NCAR - Earth Observing Laboratory https://doi.org/10.5065/D6JQ0Z6D

van den Heever, S. C., Carrió, G. G., Cotton, W. R., DeMott, P. J., & Prenni, A. J. (2006). Impacts of nucleating aerosol on Florida storms. Part I: Mesoscale simulations. *Journal of the Atmospheric Sciences*, *63*(7), 1752–1775. https://doi.org/10.1175/JAS3713.1

Varble, A. (2018). Erroneous attribution of deep convective invigoration to aerosol concentration. *Journal of the Atmospheric Sciences*, *75*(4), 1351–1368. https://doi.org/10.1175/JAS-D-17-0217.1

Webb, E. K. (1970). Profile relationships: The log-linear range, and extension to strong stability. *Quarterly Journal of the Royal Meteorological Society*, *96*(407), 67–90. https://doi.org/10.1002/qj.49709640708

Wells, K. C., Witek, M., Flatau, P., Kreidenweis, S. M., & Westphal, D. L. (2007). An analysis of seasonal surface dust aerosol concentrations in the western US (2001-2004): Observations and model predictions. *Atmospheric Environment*, *41*(31), 6585–6597. https://doi.org/10.1016/j.atmosenv.2007.04.034

Westerling, A. L., Hidalgo, H. G., Cayan, D. R., & Swetnam, T. W. (2006). Warming and earlier spring increase western U.S. forest wildfire activity. *Science*, *313*(5789), 940–943. https://doi.org/10.1126/science.1128834

Wiedinmyer, C., Akagi, S. K., Yokelson, R. J., Emmons, L. K., Al-Saadi, J. A., Orlando, J. J., & Soja, A. J. (2011). The Fire INventory from NCAR (FINN): A high resolution global model to estimate the emissions from open burning. *Geoscientific Model Development*, *4*(3), 625–641. https://doi.org/10.5194/gmd-4-625-2011

Wood, R. (2012). Stratocumulus clouds. *Monthly Weather Review*, *140*(8), 2373–2423. https://doi.org/10.1175/MWR-D-11-00121.1

Zhang, D., & Anthes, R. A. (1982). A high-resolution model of the planetary boundary layer—Sensitivity tests and comparisons with SESAME-79 data. *Journal of Applied Meteorology*, *21*(11), 1594–1609. https://doi.org/10.1175/1520-0450(1982)021<1594:AHRMOT>2.0.CO;2